DEFENCE **R&D** DÉFENSE

A Spatial Power Spectrum Estimator for Distributed Signals

W.J.L. Read
Defence Research Establishment Ottawa

National   Défense
Defence   nationale

Canada

20010705 065

DEFENCE **R&D** DÉFENSE

A Spatial Power Spectrum Estimator for Distributed Signals

W.J.L. Read
EW Sensors Group
Electronic Support Measures Section

DEFENCE RESEARCH ESTABLISHMENT OTTAWA

Project
5BD15

Abstract

This report details the development of an N-channel spatial power spectrum estimation technique called the *SPatial Incoherent Region Estimator* (SPIRE). It was developed in support of research aimed at characterizing the spatial spreading of HF signals caused by the high latitude propagation environment with the ultimate goal of improving high latitude HF radio direction finding performance. Based on the assumption of temporal and spatial incoherence, SPIRE uses a surprisingly simple, yet effective, approach based on maximum likelihood principles to model the spatial power spectrum. The result is an algorithm which provides a more accurate and more informative characterization of the spatial nature of incoming signals than currently popular conventional and modern superresolution algorithms. This characterization includes bearing, spatial extent and power distribution, and total power of the signal. It also includes total noise power and modeling accuracy. The performance and utility of the SPIRE algorithm is demonstrated using both simulation and off-air data.

Résumé

Ce rapport décrit l'élaboration d'une technique d'estimation du spectre de puissance spatial utilisant N canaux appelée SPIRE (SPatial Incoherent Region Estimator, c.-à-d. estimateur de région spatiale incohérente). Cette technique a été élaborée pour appuyer la recherche visant à caractériser l'étalement des signaux HF causé par le milieu de propagation aux hautes latitudes dans le but premier d'améliorer les performances de la radiogoniométrie HF à ces latitudes. À partir de l'hypothèse d'incohérence temporelle et spatiale, SPIRE utilise une approche étonnamment simple, mais efficace, basée sur les principes du maximum de vraisemblance, pour modéliser le spectre de puissance spatial. Le résultat est un algorithme qui permet une caractérisation plus précise et plus informative de la nature spatiale des signaux reçus que les algorithmes classiques et modernes de superrésolution qui sont actuellement répandus. Cette caractérisation porte sur le relèvement, sur la distribution de puissance et l'étendue spatiales, ainsi que sur la puissance totale du signal. Elle porte aussi sur la puissance de bruit totale et la précision de la modélisation. Les performances et l'utilité de l'algorithme SPIRE sont démontrées par simulation et par utilisation de données captées en direct.

Executive summary

The requirement exists to improve the accuracy of strategic high latitude HF direction finding (DF) systems. In the past, poor DF accuracy derived from Arctic measurements has led to low confidence in high latitude sites despite the strategic relevance of these sites for transmitter geolocation.

Disturbances in the ionosphere which scatter the signal over a range of azimuth and elevation directions (spatial spreading) are a major problem. This leads to situations which are not well modeled by currently popular DF algorithms since the signal is assumed to be cleanly reflected from the ionosphere. The result can be bearings with large biases and standard deviations.

Recently a new approach, the Spread Maximum Likelihood (SML) algorithm, was developed, incorporating a spatial spreading model. Despite improved performance compared to other DF algorithms, performance was still not as good as desired. The problem may be that the SML algorithm employs a signal scattering model requiring the spatial shape (but not size) and power density profile of the scattering region to be constant and known a priori. Not only has the optimum shape not yet been determined, there is reason to believe that, given the dynamic nature of the high latitude ionosphere, the shape of the scattering region may change significantly over time.

To understand the true nature of these scattering regions better, the SML algorithm has been radically modified to include estimation of the spatial shape and power density of the received signal. The result is a new algorithm called the *SPatial Incoherent Region Estimator* (SPIRE), which effectively maps out the spatial power spectrum of the radio sky. Surprisingly, despite the increase in number of signal parameters to be estimated, the SPIRE algorithm is much simpler and faster than the SML algorithm. In fact, the SPIRE algorithm is comparable in speed to the current generation of superresolution algorithms and is much more suited to the problem of spatially spread signals.

The development and evaluation of the performance of the SPIRE algorithm is documented in this report. The performance evaluation was carried out using both simulated and off-air data and also included comparisons with other superresolution DF algorithms.

In comparisons using simulated data, the effects of noise, spatial spreading, and the shape of the spread region were considered, as well as the ability to detect a weaker point-source (no spatial spreading) signal in the presence of a stronger spatially spread signal. For the signal conditions tested, the performance of the SPIRE algorithm was generally found to be as good as, or better than, the performances of currently popular superresolution DF algorithms.

In comparisons using off-air data collected with the Vortex system (a multi-channel HF receiver system located at CFS Alert) in 1995-96, the results were inconclusive. However, the usefulness of the SPIRE algorithm to detect problems, particularly the

ability to measure modeling error, made it possible to show that antenna mutual coupling problems had almost certainly corrupted the measurements. Ideally, mutual coupling effects could be corrected by doing advanced processing to calibrate the data; however, more research work needs to be done in this area.

W.J.L.Read. 2000. A Spatial Power Spectrum Estimator For Distributed Signals. DREO TR 2000-099. Defence Research Establishment Ottawa.

Sommaire

Il est nécessaire d'améliorer la précision des systèmes stratégiques de radiogoniométrie HF aux hautes latitudes. Par le passé, la faible précision obtenue en radiogoniométrie avec les mesures faites dans l'Arctique a mené à un bas niveau de confiance dans les sites des hautes latitudes, malgré la pertinence stratégique de ces sites pour établir la position géographique des émetteurs.

Un problème majeur est lié aux perturbations ionosphériques qui diffusent le signal sur une gamme de directions en azimut et en site (étalement spatial). Il en résulte des situations qui ne sont pas bien modélisées par les algorithmes de radiogoniométrie actuellement répandus, étant donné que le signal est considéré par hypothèse comme étant nettement réfléchi par l'ionosphère. Les relèvements obtenus peuvent alors comporter des biais et des écarts-types importants.

Récemment, un nouvel outil, l'algorithme à vraisemblance maximale étalée (SML), comprenant un modèle d'étalement spatial, a été élaboré. Bien que cet algorithme soit plus efficace que les autres algorithmes de radiogoniométrie, l'efficacité désirée n'était pas encore atteinte. Le problème peut être dû au fait que l'algorithme SML utilise un modèle de diffusion du signal dans lequel la forme spatiale (mais pas la taille) et le profil de densité de puissance de la région de diffusion doivent être constants et connus a priori. Non seulement la forme optimale n'a pas encore été déterminée, mais on est justifié de croire qu'en raison de la nature dynamique de l'ionosphère aux hautes latitudes, la forme de la région de diffusion peut changer beaucoup avec le temps.

Pour mieux comprendre la nature réelle de ces régions de diffusion, on a modifié radicalement l'algorithme SML de façon à y inclure une estimation de la forme spatiale et de la densité de puissance du signal reçu, ce qui a donné un nouvel algorithme appelé SPIRE (SPatial Incoherent Region Estimator, c.-à-d. estimateur de région spatiale incohérente), qui représente efficacement le spectre de puissance spatial de la propagation radio ionosphérique. Étonnamment, en dépit de l'accroissement du nombre de paramètres de signaux à évaluer, l'algorithme résultant est beaucoup plus simple et plus rapide que l'algorithme SML, avec une vitesse comparable à celle des algorithmes de superrésolution de la génération actuelle, mais beaucoup mieux adapté au problème des signaux à étalement spatial.

L'élaboration de l'algorithme SPIRE est documentée dans ce rapport et ses performances sont évaluées à l'aide de données simulées. Cette évaluation tient compte des effets du bruit, du degré d'étalement spatial et de la forme de la région d'étalement. Elle permet aussi de détecter un signal de source ponctuelle (pas d'étalement spatial) faible en présence de signaux à étalement spatial plus forts.

Dans les comparaisons effectuées à l'aide de données simulées, les performances de l'algorithme SPIRE se sont généralement révélées égales ou supérieures à celles des algorithmes de radiogoniométrie actuellement répandus, pour les diverses conditions de signaux ayant fait l'objet d'essais.

Dans les comparaisons effectuées à l'aide de données en direct recueillies avec le système de réception HF multivoie Vortex à la SFC Alert en 1995-1996, les résultats n'étaient pas concluants. Cependant, l'utilité de l'algorithme SPIRE pour détecter les problèmes, en particulier la capacité de mesurer l'erreur de modélisation, a permis de montrer que les problèmes de couplage mutuel d'antenne avaient presque certainement corrompu les mesures. Idéalement, les effets du couplage mutuel pourraient être corrigés par un traitement évolué servant à étalonner les données, mais d'autres travaux de recherche sont nécessaires dans ce domaine.

W.J.L.Read. 2000. Une technique d'estimation du spectre de puissance spatial pour les signaux distribués. DREO TR 2000-099. Centre de recherches pour la défense, Ottawa.

Table of contents

List of figures

List of tables

1. INTRODUCTION

The requirement exists to improve the accuracy of strategic HF direction finding systems, particularly in the Arctic. In the past, poor direction finding (DF) accuracy derived from Arctic measurements has led to low confidence in high latitude sites despite the strategic relevance of these sites for transmitter geolocation.

Patches of enhanced electron density and associated instabilities in the F layer of the ionosphere, which drift across the polar cap during darkness in a roughly antisunward direction at speeds ranging from a few hundreds to over one thousand meters per second [1], are a major problem. These patches can cause scattering of a signal from azimuth directions which are very different from the true bearing of the transmitter.

One avenue of investigation being pursued is the development of new DF algorithms which are better matched to the high latitude HF signal environment. Currently popular DF algorithms assume that the incoming signal can be modeled as a point source, or equivalently, that the incoming radio signal has a planar wavefront. This is reasonable if the size of the transmission source is extremely small relative to its range, the size of the DF array is also small relative to the transmitter range, the ionosphere acts as a perfect or near-perfect reflector, and local site multipath can be ignored. Unfortunately, at high latitudes, during periods when scattering from large moving patches occurs, the received signal arrives from a range of bearings in both azimuth and elevation. In this report, signals of this type are called spread-source signals. Typical modern DF algorithms estimate a spread-source signal as being a cluster of several point-source signals coming from the same direction.

Although representation of a spread-source signal as a cluster of several point-source signals is useful, the information provided is degraded. For example, it becomes more difficult to: determine the spatial extent of the signal; determine if two or more similar bearing estimates represent different reflection paths or a single scattering region of the ionosphere; and, detect and estimate the direction of weaker signals. Solving this latter difficulty is important since a previous study [2] has shown that sporadic-E propagation, when it exists and can be measured, leads to good bearing estimates. Hence, it is important that a DF algorithm be able to detect and determine the bearing of a weaker sporadic-E reflected signal in the presence of one or more stronger F-region signals.

Recently a new approach, the Spread Maximum Likelihood (SML) algorithm [3], was developed, incorporating a spatial spreading model to handle scattering effects due to the ionosphere. Despite improved performance compared to other DF algorithms [1], [3], [4], performance was still not as good as desired. The problem may be that this new algorithm employs a signal scattering model requiring the shape (but not size) and power density profile of the scattering region to be constant and known a priori. Not only has the optimum shape not yet been determined, there is reason to believe that, given the dynamic nature of the high latitude ionosphere, the shape of the scattering region may change significantly over time.

To understand the true nature of these scattering regions better, the SML algorithm has been radically modified to include estimation of the spatial shape and power density of the received signal. The result is a new algorithm called the *SPatial Incoherent Region Estimator* (SPIRE), which effectively maps out the spatial power spectrum of the radio sky. Surprisingly, despite the increase in number of signal parameters to be estimated, the SPIRE algorithm is much simpler and faster than the SML algorithm. In fact, the SPIRE algorithm is comparable in speed to the current generation of superresolution algorithms and is much more suited to the problem of spatially spread signals, as will be shown through simulation.

An unexpected bonus of the SPIRE algorithm approach is a function which effectively measures the modeling error. This error function provides a useful way to determine proper sampling size, and whether local multipath/coupling effects may be degrading the results. This is demonstrated using high latitude HF data collected with the Vortex system (an experimental 12 channel HF collection system) in 1995-96 at CFS Alert.

The layout of the rest of the report is as follows. In Section 2, the underlying maximum likelihood approach is discussed and the appropriate cost and model error functions are introduced. This is followed by the development of a signal model which reduces the estimation problem to calculation of the signal and noise power parameters only. In Section 3, the basic algorithmic procedure for signal and noise power parameter estimation is developed. In Section 4, problems with spatial ambiguities are dealt with through the adoption of a "simpler is better" guideline. An implementation scheme is also introduced which leads to significantly faster processing. Additionally issues, such as sample size and maximum number of signals, are also addressed. In Section 5, simulated data is used to compare the performance of the SPIRE algorithm with other popular DF algorithms. In Section 6, performance is again compared using off-air data. This data is also processed to show the usefulness of measuring modeling error for sample size determination and mutual coupling/local site multipath detection. Finally, in Section 7, the conclusions and recommendations are presented.

2. DEVELOPMENT OF THE SPIRE ALGORITHM

2.1 Maximum Likelihood Estimation

A successful, albeit often computationally intensive, approach to estimation is based on the maximum likelihood method. Essentially the idea is to find the most likely state of a signal process given a set of measurement observations made of the process. Since this is a statistical approach, the method applies to cases where the signal generation is a random process and/or the measurements have been corrupted by additive noise (which is a random process).

Assuming the random processes are all normally Gaussian distributed, and measurements are made using N sensors, the associated probability density function is given by [5]

$$(1) \qquad f(\mathbf{x}_0, \mathbf{x}_1, ..., \mathbf{x}_{K-1}) = \frac{1}{[\pi^N \det \mathbf{C}]^K} e^{-\mathrm{trace}((\mathbf{X}-\mathbf{M})^H \mathbf{C}^{-1}(\mathbf{X}-\mathbf{M}))}$$

where the superscript H denotes the conjugate-transpose operation, and the vectors $\mathbf{x}_0, ..., \mathbf{x}_{K-1}$ represent the random complex measurement data associated with all N sensors for time instances $t = t_0, t_1, ..., t_{K-1}$ as defined by

$$(2) \qquad \mathbf{x}_k = \begin{bmatrix} x_0(k) \\ x_1(k) \\ x_2(k) \\ \vdots \\ x_{N-1}(k) \end{bmatrix} \qquad \text{for } 0 \leq k < K.$$

Additionally, the matrix $\mathbf{X}$ represents all K measurement vectors as given by

$$(3) \qquad \mathbf{X} = [\mathbf{x}_0, \mathbf{x}_1, ..., \mathbf{x}_{K-1}],$$

the matrix $\mathbf{M}$ represents the corresponding mean values of the measurements, and $\mathbf{C}$ is the $N \times N$ covariance matrix describing the correlations among sensors. The exact definitions of the matrices $\mathbf{M}$ and $\mathbf{C}$ depend on how the above density function is applied to the particular estimation problem to be solved, as will be seen. Once these definitions have been set up, the maximum likelihood solution is found by maximizing the probability density function with the most appropriate valid choices of $\mathbf{M}$ and/or $\mathbf{C}$. These maximizing choices for $\mathbf{M}$ and/or $\mathbf{C}$ can then be related back to the signal parameters of interest.

For direction finding purposes, $\mathbf{x}_1, ..., \mathbf{x}_{K-1}$ are taken to represent the complex baseband outputs from an array of N antennas. The definitions for $\mathbf{M}$ and $\mathbf{C}$ depend on the assumptions made about the signals. Given that man-made HF signals are bounded (finite power) and any constant modulus properties will be destroyed by the dynamic nature of the ionosphere (e.g. fading and Doppler spreading), it is reasonable to model

these signals as being zero-mean stochastic processes. Hence this leads to the assumptions that

$$(4) \qquad\qquad \mathbf{M} = \mathbf{0}$$

where $\mathbf{0}$ is a matrix of all zeros, and

$$(5) \qquad c_{mn} = E[x_m(k)x_n(k)^*] \quad \text{for} \ \ 0 \le k < K \ \text{and} \ 0 \le m,n < N$$

c_{mn} is the element of $\mathbf{C}$ located in the mth row and the nth column.

2.2 The Cost and Model Error Functions

The probability density function (1) can be simplified using (4) to give

$$(6) \qquad f(\mathbf{x}_0, \mathbf{x}_1, ..., \mathbf{x}_{K-1}) = \frac{1}{[\pi^N \det \mathbf{C}]^K} e^{-\text{trace}(\mathbf{X}^H \mathbf{C}^{-1} \mathbf{X})}$$

The objective is to find the unknown covariance matrix $\mathbf{C}$ which maximizes this expression. This is equivalent to maximizing the cost function $L_c = \ln f(\mathbf{x}_0, \mathbf{x}_1, ..., \mathbf{x}_{K-1})$ or,

$$(7) \qquad L_c = -NK \ln(\pi) - K \ln(\det \mathbf{C}) - \text{trace}(\mathbf{X}^H \mathbf{C}^{-1} \mathbf{X}).$$

Since the addition or multiplication by a constant value has no effect on the maximization, the cost function can be simplified to

$$(8) \qquad L = -\ln(\det \mathbf{C}) - \text{trace}(\mathbf{R}\mathbf{C}^{-1})$$

where $\mathbf{R}$ is the *data covariance matrix* constructed from $\mathbf{X}$ using

$$(9) \qquad \mathbf{R} = \frac{1}{K}\mathbf{X}\mathbf{X}^H.$$

Although not required for the theoretical development of the SPIRE algorithm, the cost function can modified to provide a measure of the modeling error which, in turn, provides information about the quality of the estimates. A simple model error function can be defined as

$$(10) \qquad \varepsilon = L_{max} - L$$

where L_{max} is the cost function value when the model covariance matrix exactly matches the data covariance matrix, or $\mathbf{C} = \mathbf{R}$. Expanding the expression for ε in terms of (8) and simplifying, then

$$(11) \qquad \varepsilon = \ln(\det \mathbf{C}) + \text{trace}(\mathbf{R}\mathbf{C}^{-1}) - \ln(\det \mathbf{R}) - N$$

The usefulness of ε is shown later on in Sections 4, 5 and 6.

2.3 Modeling the Signal Environment

The modeling aspect comes into play when $\mathbf{C}$ is being selected. A model is used to generate $\mathbf{C}$ based on input modeling parameters such as, for example, the number of signals, signal bearings, signal amplitudes/powers, and noise powers. For this reason, $\mathbf{C}$ is referred to as the *model covariance matrix* in this report.

The procedure for determining the optimum choice for $\mathbf{C}$ (i.e. the choice which maximizes the cost function L) starts by choosing initial model parameters, generating the corresponding model covariance $\mathbf{C}$, and then determining the cost function value L. The model parameters are then successively refined and $\mathbf{C}$ recomputed until the maximum cost function value has been achieved. The model parameter values corresponding to this maximum value are then taken to be the optimum or maximum likelihood estimates.

The particular model used to generate the model covariance matrix depends on many factors including the transmitter(s) and receiver characteristics, the signal propagation environment, the noise sources, and so on. One way to set this model up, is to consider the generation of synthetic data which imitates the collected data, and then use this synthetic data to determine $\mathbf{C}$ according to

$$\text{(12)} \qquad \mathbf{C} = \frac{1}{K}\mathbf{Y}\mathbf{Y}^H$$

where $\mathbf{Y}$ is the matrix of model data and has the same form and dimensions as $\mathbf{X}$.

Based on these simplifying assumptions, the received signal can be decomposed as

$$\text{(13)} \qquad \mathbf{Y} = \mathbf{Y}_1 + \mathbf{Y}_2 + ... + \mathbf{Y}_M + \mathbf{N}$$

where the matrices $\mathbf{Y}_1, \mathbf{Y}_2, ..., \mathbf{Y}_M$ represent the model data for the M individual signals, and $\mathbf{N}$ is the modeled noise. The matrix $\mathbf{Y}_m$, for $0 < m \le M$, can be defined in vector form as

$$\text{(14)} \qquad \mathbf{Y}_m = \mathbf{e}_m \mathbf{a}_m^H$$

where $\mathbf{e}_m$ is the steering vector (or array response vector) for the mth signal, and $\mathbf{a}_m$ is the corresponding signal amplitude vector. The definitions for the elements of the steering vector are given by

$$\text{(15)} \qquad \mathbf{e}_m = \frac{1}{\sqrt{N}} \begin{bmatrix} e^{j\frac{2\pi}{\lambda}(x_0 \sin\phi_m \cos\psi_m + y_0 \cos\phi_m \cos\psi_m)} \\ e^{j\frac{2\pi}{\lambda}(x_1 \sin\phi_m \cos\psi_m + y_1 \cos\phi_m \cos\psi_m)} \\ \vdots \\ e^{j\frac{2\pi}{\lambda}(x_{N-1} \sin\phi_m \cos\psi_m + y_{N-1} \cos\phi_m \cos\psi_m)} \end{bmatrix}$$

where λ is the signal wavelength, x_n and y_n are the Cartesian coordinates for antenna n (with the phase center of the array located at the origin), ϕ_m is the azimuth angle of the mth signal measured clockwise with respect to the Y-axis of the coordinate system, and

ψ_m is the elevation angle measured with respect to the X-Y plane (the ground). The definition for the elements of the signal amplitude vector is given by

$$(16) \qquad \mathbf{a}_m = \begin{bmatrix} a_m^*(0) \\ a_m^*(1) \\ \vdots \\ a_m^*(K-1) \end{bmatrix}$$

The coefficients $a_m(0), a_m(1), ..., a_m(K-1)$ are the received complex amplitudes of the mth signal for time instances $t_0, t_1, ..., t_{K-1}$.

The model covariance can also be written as a sum of the noise covariances, the signal covariances, and the signal cross-covariances, or

$$(17) \qquad \mathbf{C} = \sigma^2 \mathbf{C}_\eta + \sum_{m=1}^{M} \mathbf{C}_{mm} + \sum_{m=1}^{M-1} \sum_{n=m+1}^{M} (\mathbf{Q}_{mn} + \mathbf{Q}_{mn}^H)$$

where σ^2 is the noise power, $\mathbf{C}_\eta$ is the normalized noise covariance matrix (trace $\mathbf{C}_\eta = 1$), $\mathbf{C}_{mm}$ is the signal covariance matrix for the mth signal, and $\mathbf{Q}_{mn}$ is the signal cross-covariance matrix. The generation of these matrices is discussed in the following paragraphs.

The noise covariance matrix $\mathbf{C}_\eta$ is assumed to be known a priori and will not be considered as part of the estimation process. The determination of $\mathbf{C}_\eta$ can be done either through theoretical statistical considerations, or through measurements. For example, if the noise is known to be white Gaussian in nature with equal but uncorrelated amplitudes in each channel, then $E[\eta_m(k)\eta_m^*(k)] = \sigma^2$ and $E[\eta_m(k)\eta_n^*(k)] = 0$ for $0 \le m, n < N$ and $m \ne n$, hence

$$(18) \qquad \mathbf{C}_\eta = \frac{1}{N}\mathbf{I}_N$$

where $\mathbf{I}_N$ is the $N \times N$ identity matrix. Alternatively, if data measurements can be taken when no signals are present, then

$$(19) \qquad \mathbf{C}_\eta = \frac{\mathbf{X}\mathbf{X}^H}{\text{trace}(\mathbf{X}\mathbf{X}^H)}.$$

More elaborate procedures could be developed involving a number of measurement sets with the same noise environment but different signal directions, however the development of this kind of approach is beyond the scope of this report. It suffices to say that joint estimation of both the noise and signal characteristics should be avoided if possible since it leads to poorer accuracy.

The signal covariance matrix $\mathbf{C}_{mm}$ can be defined in terms of the model data as

$$(20) \qquad \mathbf{C}_{mm} = \frac{1}{K}\mathbf{Y}_m\mathbf{Y}_m^H$$

which can be further expanded in terms of the component amplitude and steering vectors as

$$(21) \qquad \mathbf{C}_{mm} = \frac{\mathbf{a}_m^H \mathbf{a}_m}{K} \mathbf{e}_m \mathbf{e}_m^H.$$

In a similar fashion, the cross-covariance matrix $\mathbf{Q}_{mn}$ can also be defined and expanded to get

$$\mathbf{Q}_{mn} = \frac{1}{K} \mathbf{Y}_m \mathbf{Y}_n^H$$

$$(22) \qquad \qquad = \frac{\mathbf{a}_m^H \mathbf{a}_n}{K} \mathbf{e}_m \mathbf{e}_n^H \qquad \text{for } n > m.$$

For the high latitude HF skywave environment, the assumption is made that the cross-covariance terms disappear. This is based on considering the various cases. Signals from different transmitters will be uncorrelated. Signals originating from the same transmitter but reflected off different layers of the ionosphere will also be uncorrelated due to the large path length differences usually encountered (i.e., the path delay time differences will be greater than the inverse bandwidth of the signal). Signals originating from the same transmitter but scattered from different parts of the same region (or patch) of the ionosphere will also be uncorrelated since the scattering elements within the region are short-lived [11]. Given Doppler spread measurements for patch scattered signals of up to 40 Hz [10]), it is further assumed that this is caused by the birth/death rate of the scatterers giving a decorrelation time of $\tau > 1/40s$. More generally, if the Doppler spread is caused by turbulent motion of the electron gas plasma of the ionosphere, from the perspective of the receiver, the results come to the same thing (i.e. $\tau > 1/40s$).

A violation of the assumption of uncorrelated signals is the case of local site multipath. However, like the problem of determining the noise correlations, including the signal correlations in the estimation process is highly undesirable (although in the standard stochastic ML approach this is done [8]). Hence it is assumed that either the receiver site is well chosen, or signal correlations can be determined independently and corrected as done, for example, in [9].

The end result is that (17) can be simplified to become

$$(23) \qquad \mathbf{C} = \sigma^2 \mathbf{C}_\eta + \sum_{m=1}^{M} \mathbf{C}_{mm}$$

The great advantage of this form is that the signal part of the model covariance matrix can be generated as the sum of the individual signal covariance matrices. More importantly, by dividing the regions of interest into sufficiently small subregions, each subregion can be represented by a single scattering element or point source leading to

$$(24) \qquad \mathbf{C} = \sigma^2 \mathbf{C}_\eta + \sum_{m=1}^{M} s_m \, \mathbf{e}_m \mathbf{e}_m^H$$

where $\mathbf{e}_m$ represents the steering vector associated with the bearing of the mth subregion and s_m is the corresponding signal power.

The optimum solution for σ^2 and s_m for $m = 1, ..., M$ is found by choosing the values which maximize the cost function L. If the region to be subdivided is the entire field-of-view of the antenna array, then the result will be a maximum likelihood estimate of the spatial power spectrum where **no** assumptions have been made about the shape and power distribution of the scattering region(s), nor any assumption about the number of signals (a value required by most superresolution methods).

On the face of it, given M will be very large (e.g. for a 1° uniform spacing over both $0 - 360^\circ$ in azimuth and $0 - 90^\circ$ in elevation then $M = 32400!$), there would appear to be two fatal objections to the proposed approach. The first objection is that the model seems to be over-determined (too many model parameters) so that many different and incorrect solutions will exist. The second objection is that estimation of so many parameters will make the method computationally slow. However, the fact that the model parameters are constrained so that $\sigma^2, s_m \geq 0$, plus the reduction in the number of kinds of parameters (i.e. power only versus the power, bearing, and bearing spread parameters of the SML algorithm) has a major impact on overcoming these objections as will be seen in later sections.

3. MODEL PARAMETER ESTIMATION

As indicated previously, optimization of the power parameters σ^2 and $s_1, ..., s_M$ proceeds in a way which maximizes the cost function L. The basic algorithm begins by initializing the noise and signal power parameters, and then iteratively updates these parameters using a gradient technique until a sufficiently accurate result is achieved. The basic algorithm is listed below. Additional details for some of the steps listed can be found in the indicated sections.

1. Initialize model noise power by performing an eigendecomposition on the whitened data covariance matrix to get

$$(25) \qquad \mathbf{C}_\eta^{-\frac{1}{2}} \mathbf{R} \mathbf{C}_\eta^{-\frac{1}{2}} = \sum_{i=1}^{N} \lambda_i \mathbf{v}_i \mathbf{v}_i^H$$

and then overestimating the initial value of σ^2 using

$$(26) \qquad \sigma^2 = 2\lambda_N$$

(Section 3.1).

2. Initialize the model signal powers by setting

$$(27) \qquad s_1 = s_2 = \cdots = s_M = \frac{1}{N}(\mathrm{trace}\,\mathbf{R} - \sigma^2)$$

(Section 3.2).

3. Initialize the loop counter: $loop = 0$

4. Increment the loop counter: $loop \rightarrow loop + 1$

5. Update signal power parameter estimates (Section 3.3).

6. While $loop < max\_loop$ go to step 4.

7. (Optional) Update noise power parameter (Section 3.4).

8. Output model parameter estimates.

A value of $max\_loop = 20$ has been found to give good results. Enhancements to accelerate the processing speed and appropriate choices for the various algorithm control parameters are discussed in Section 4.

3.1 Initial Noise Power Estimate

The initial estimate of the noise power σ^2 is based on the idea that, in the presence of spatially white Gaussian noise, the data covariance matrix can be divided into signal and noise subspaces. In the derivations thus far, the noise has not been assumed to be white, but it has been assumed to be known. Hence the first step is to whiten the noise by performing the following modification to the data covariance matrix.

$$(28) \qquad \mathbf{R}_w = \mathbf{W}^H \mathbf{R} \mathbf{W}$$

where

$$(29) \qquad \mathbf{W} \mathbf{W}^H = \mathbf{C}_\eta^{-1}$$

There are many equally valid solutions for $\mathbf{W}$ which satisfy (29) but for simplicity of notation the choice

$$(30) \qquad \mathbf{W} = \mathbf{C}_\eta^{-\frac{1}{2}}$$

has been used. The actual choice is a matter of convenience. Additionally, in the special case where the noise is already white and Gaussian, then

$$(31) \qquad \mathbf{R}_w = N\mathbf{R}$$

Using eigendecomposition, the whitened data covariance matrix can be represented by

$$(32) \qquad \mathbf{R}_w = \sum_{i=1}^{N} \lambda_i \mathbf{v}_i \mathbf{v}_i^H$$

where $\lambda_1, ..., \lambda_N$ are the eigenvalues ordered so that $\lambda_1 \geq \cdots \geq \lambda_N$, and $\mathbf{v}_1, ...\mathbf{v}_N$ are the corresponding orthonormal eigenvectors. In the ideal case, $\mathbf{R}_w$ is formed from an infinite number of sensor snapshots, there are $M < N$ point-source signals impinging on the array, and the measurements are corrupted by additive white Gaussian. Under these conditions, the first M eigenvectors will be associated with signal + noise, while the rest ($N - M$ eigenvectors) will be associated with noise only. The corresponding values of the $N - M$ smallest eigenvalues will all equal σ^2. Under these ideal conditions, estimating σ^2 from any of the smallest $N - M$ eigenvalues is a trivial exercise.

In the high latitude HF case, the number of measurements will not be infinite, and the signals will not be point-source (due to azimuth/elevation spreading). For a limited number of point-source signals, the problem of finite samples could be solved by averaging the smallest $N - M$ eigenvalues to produce an estimate of the noise power. The problem of spatial spreading cannot be solved so easily, however, since spreading causes the effective value of M (remembering that M is the number of *point-source* signals) to increase so that it may exceed N. Figure 1 illustrates this point through simulation. Figure 1a shows the spatial power spectrum consisting of a point-source signal, a spread-source signal, and a noise floor set to yield a signal-to-noise ratio

(SNR) of 20 dB. Figure 1b shows the corresponding eigenvalues for three cases: signal only; noise only; and signal plus noise. The antenna array configuration used for the simulation is shown in Figure 2 and discussed in Section 4.1. The results demonstrate that, in this case, the signal power affects all the eigenvalues implying $M \geq N$ even thought there were only two signals.

The simplest solution to the spreading problem is to assume that at least one of the dimensions of $\mathbf{R}_w$ is dominated by noise. The noise power can then be estimated as,

$$(33) \qquad \qquad \sigma^2 = \lambda_N$$

For the example in Figure 1, choosing the smallest eigenvalue for the noise power estimate gives the best result even though it is slightly overestimated.

In cases where the signal power dominates all dimensions of $\mathbf{R}_w$ (e.g., in the previous example this would be true for an SNR = 30 dB), then λ_N will be a large overestimate of σ^2. In practice, this overestimate has not been found to significantly affect the accuracy of the signal estimates (which are of most interest), so no attempt has been made to investigate this problem further.

In fact, it has been found that purposely overestimating the noise power by a factor of two, and then fixing this value until after the final iteration of the SPIRE algorithm, leads to more accurate estimates of the noise power and better detection of weaker signals. If the noise power is updated within the loop, the signal model sometimes adapts to the noise (due to the signal model's greater flexibility) forcing the estimated noise power to zero and causing false signal estimates. Under these circumstances convergence occurs on an undesirable false maximum of the cost function. Hence it is better to wait until the signal model estimate has stabilized before fine tuning the noise power.

3.2 Initial Signal Power Estimate

The initial signal powers are set equal according to

$$(34) \qquad \qquad s_1 = s_2 = \cdots = s_M = s$$

Since the total power observed in the data is assumed to be produced by uncorrelated processes, then ideally

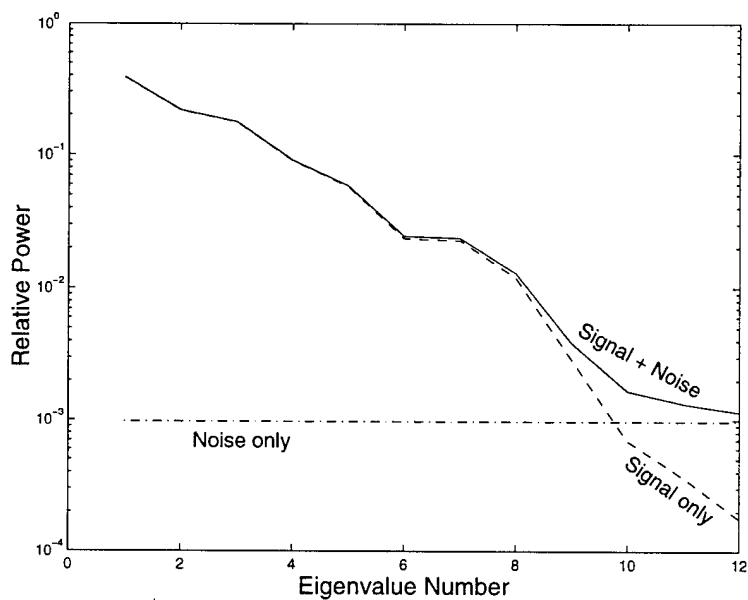$$(35) \qquad \qquad \mathrm{trace}\mathbf{R} = \sigma^2 + \sum_{m=1}^{M} s_m$$

Hence, given the signal powers are all equal, the quantity s is given by

$$(36) \qquad \qquad s = \frac{1}{M}(\mathrm{trace}\mathbf{R} - \sigma^2)$$

where the value for σ^2 used here is the initial value computed according to (33).
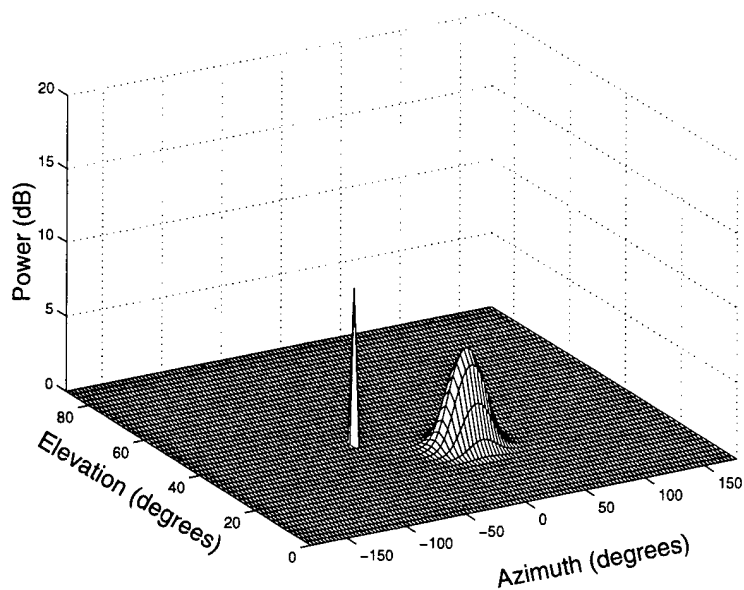
(a)

(b)

Figure 1: *Simulation of a spread-source signal environment showing (a) the spatial power spectrum, and (b) the corresponding eigenvalues when an array with 12 antennas is used.*

For a limited sample of sensor data, (36) will only be approximately true and a more accurate value of s could be obtained by maximizing the cost function L. However, for the sake of initialization, and in the interests of reducing the number of computations, (36) is sufficient.

3.3 Signal Power Estimates

The optimum solution for the signal power s_m can be found by setting the gradient of L to zero where the gradient is measured with respect to s_m. The generic gradient of the cost function L (derived in [3]) is given by

$$(37) \qquad G(\alpha) = \text{trace}\left((\mathbf{C}^{-1}\mathbf{R} - \mathbf{I})\mathbf{C}^{-1}\frac{\partial \mathbf{C}}{\partial \alpha} \right)$$

In the case where $\alpha = s_m$, setting the gradient $G(s_m)$ to zero leads to the following expression (based on the derivation in [3] with some slight rearranging),

$$(38) \qquad \Delta s_m = \frac{\mathbf{e}_m^H(\mathbf{C}^{-1}\mathbf{R} - \mathbf{I})\mathbf{C}^{-1}\mathbf{e}_m}{(\mathbf{e}_m^H\mathbf{C}^{-1}\mathbf{e}_m)^2}.$$

where Δs_m is the estimated signal update. Hence for a particular signal source m, $s_m + \Delta s_m$ is the updated signal power which maximizes L.

For computational efficiency, the signal power updates for $m = 1, ..., M$ are done in parallel so that the matrices $\mathbf{C}^{-1}$ and $(\mathbf{C}^{-1}\mathbf{R} - \mathbf{I})\mathbf{C}^{-1}$ need only be calculated once, and not M times for each individual signal power update. However, this results in an overestimation of the signal updates so a compensating scaling factor is required. Calling the scaling factor μ, the update is applied as: $s_m \rightarrow s_m + \mu\Delta s_m$.

To ensure the fastest convergence using this approach, the value of μ which maximizes L is calculated for each iteration. As no direct solution has been found, the bisection method has been chosen as providing a reasonably fast search procedure to determine the desired solution. Using the generic search parameter α, this method is shown below.

1. Set the upper and lower search bounds, α_{low} and α_{high}.

2. Estimate the search parameter as: $\alpha = \frac{1}{2}(\alpha_{low} + \alpha_{high})$

3. Compute the gradient $G(\alpha)$.

4. If $G(\alpha) \geq 0$ then $\alpha_{low} = \alpha$, otherwise $\alpha_{high} = \alpha$.

5. Repeat steps 2-5 nine more times.

Steps 2-5 can be repeated more times for greater accuracy, however in practice, the number of times indicated has been found to be sufficient for the use of the SPIRE algorithm.

The appropriate model for the updated covariance matrix is

$$C = \sigma^2 C_\eta + \sum_{m=1}^{M} s_m \, \mathbf{e}_m \mathbf{e}_m^H + \mu \sum_{m=1}^{M} \Delta s_m \mathbf{e}_m \mathbf{e}_m^H \tag{39}$$

Note that the matrix formed from the first two terms on the right hand side of this expression represents the model covariance before updating and only needs to be calculated once, not in every iteration of the bisection method. Using this model and solving (37) with respect to μ, the corresponding gradient function is given by

$$G(\mu) = \sum_{i=m}^{M} \Delta s_m \mathbf{e}_m^H (C^{-1} R - I) C^{-1} \mathbf{e}_m \tag{40}$$

Finally, the search limits for μ are given by: $\mu_{low} = 0$ and $\mu_{high} = 1$.

In the event that $s_m + \mu \Delta s_m < 0$, s_m is assigned a value of zero since the signal powers can never be negative. Additionally, in the event that $s_k = 0$ and $\Delta s_k < 0$, the calculation involving $m = k$ in (39) can be ignored reducing the overall number of computations.

There are two problems with the bisection method as described here: the function $G(\mu)$ is not guaranteed to be monotonically decreasing in the region of interest; and the method does not take into account the constraint $s_m + \mu \Delta s_m \geq 0$. In practice, provided that calculations associated with obviously negative powers are eliminated (i.e. $s_k = 0$ and $\Delta s_k < 0$), the bisection method returns an answer for μ which, although not always optimum, is sufficiently good for practical purposes.

3.4 Noise Power Update

The noise power update σ^2 can also be calculated using the bisection method outlined in Section 3.2. The model covariance defined in (24) is suitable for these purposes. This definition is repeated here as

$$C = \sigma^2 C_\eta + s_m \sum_{i=1}^{M} \mathbf{e}_i \mathbf{e}_i^H \tag{41}$$

Using this model and solving (37) with respect to σ^2, the gradient function is given by

$$G(\sigma^2) = \text{trace} \left((C^{-1} R - I) C^{-1} C_\eta \right) \tag{42}$$

The lower search limit for σ^2 is $\sigma^2_{low} = 0$. The upper search limit is given by

$$\sigma^2_{high} = \text{trace } R \tag{43}$$

where trace R is an estimate of the signal plus noise power (and hence an overestimate for the noise power).

As discussed earlier in Section 3.1, the noise power update is only applied after the signal model estimates have been refined and only if a more accurate estimate of the noise power is desired.

4. IMPLEMENTATION ISSUES

To investigate some of the practical issues associated with the implementation of the SPIRE algorithm, a series of simulations were carried out. The details of the simulations are discussed in the next section (Section 4.1). The implementation issues addressed, including spatial ambiguities, signal model grid spacing, data sample size, and limitation on the number of signals, are discussed in Sections 4.2-4.5.

4.1 Simulations Settings

For these simulations, the antenna array shown in Figure 2 was chosen, as this array geometry was investigated in [16], [4] and was found to have very good characteristics for direction finding. Assuming an ideal free space response, then for any given signal bearing, the azimuth beamwidth of the array is relatively constant with respect to the azimuth bearing but varies with the elevation bearing according to

$$(44) \qquad \phi_{BW} = 7.8^\circ / |\cos\psi| \quad \text{for } |\psi| < 90^\circ$$

where the beamwidth is defined as the angular width of the main lobe of the antenna array gain pattern measured at the 3 dB points (i.e. the points at $0.707 \times$ the maximum gain). Note that measuring the azimuth beamwidth at or near $\psi = 90^\circ$ is effectively meaningless.

The elevation beamwidth is given by

$$(45) \qquad \psi_{BW} = 7.8^\circ / |\sin\psi| \quad \text{for } |\psi| > 30^\circ.$$

For elevation bearings below 30°, the beamwidth is somewhat more complicated as shown in Figure 3. The failure of the above expression at the lower elevation angles is due to the distortion of the main lobe in the antenna pattern at the elevation angle ψ by the reflection of this lobe at the elevation angle $-\psi$. For example, a 2-dimensional x-y array, using the free space assumptions, has a symmetrical gain pattern for elevation angles above and below the horizon, i.e., a main lobe and a reflection lobe. At low signal elevations, the main and reflection lobes begin to join. They are considered merged when the minimum gain between the two lobes is greater than $0.707 \times$ the maximum gain. Using the array configuration shown, this occurs at 21.2°. At this point, the beamwidth effectively doubles. For even lower signal elevations the merged lobes move closer together so the beamwidth actually decreases.

The simulation signal model was set up using two signals with the spatial power spectrum shown in Figure 4. The spread-source at $(\phi, \psi) = (10^\circ, 30^\circ)$ had a total power three times that of the point-source. The noise power level (represented by the floor at 0 dB in Figure 4) was set to be 20 dB less than the point-source signal power.

The basic steps of the SPIRE algorithm were outlined in the previous section. Following these steps, the result of processing simulated data using a subregion size of
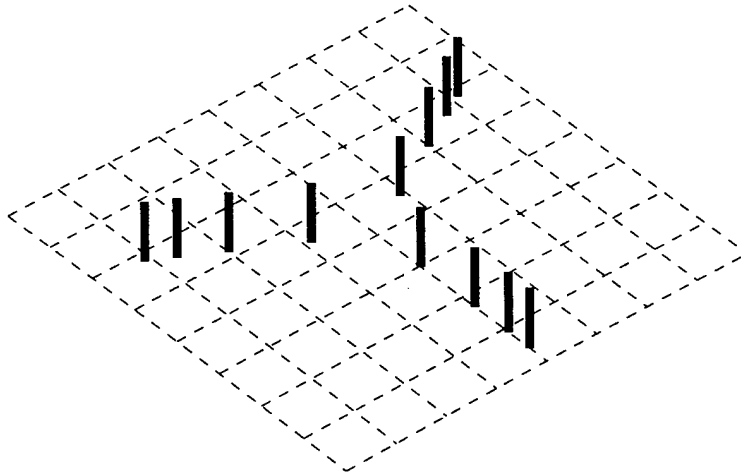
Figure 2: *Three dimensional view of the antenna array. Each grid square has a dimension of* $1\lambda \times 1\lambda$.
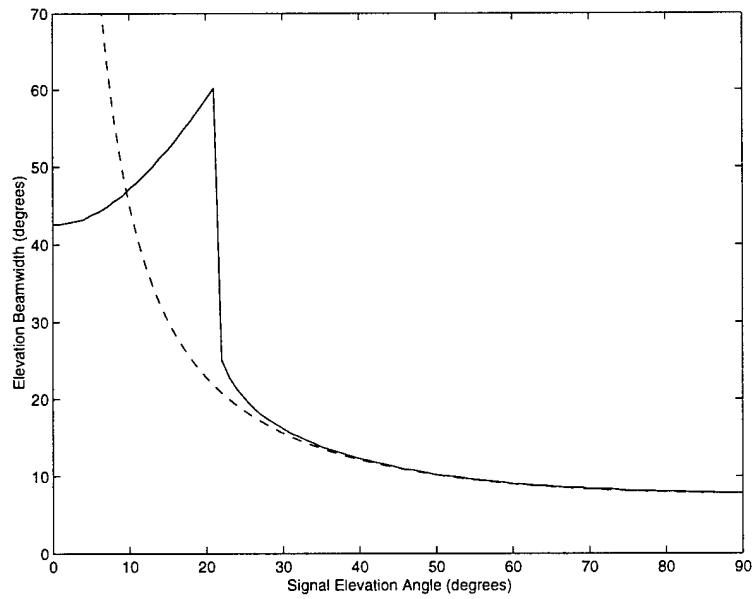

Figure 3: *Antenna array elevation beamwidth as a function of elevation comparing the simulated response (solid line) with the* $\sin^{-1} \psi$ *predicted response (dashed line).*
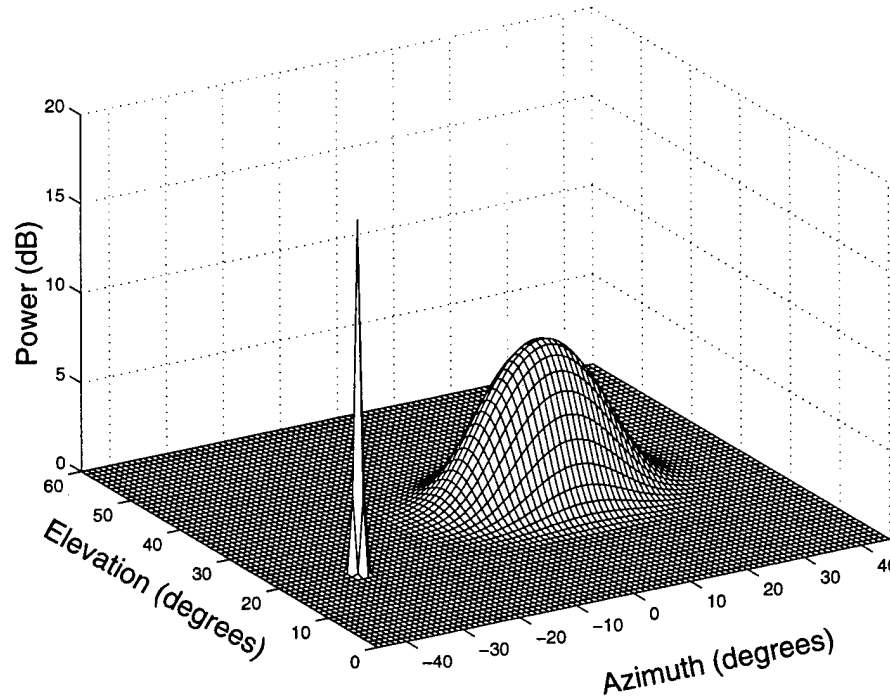
**Figure 4:** *Spatial power spectrum of signal model used for simulations.*

$1° \times 1°$ (i.e. the model covariance matrix was constructed from point source signals placed every degree in azimuth and every degree in elevation) and a sample size of $K = 10000$ is shown plotted in Figure 5a. Despite the large amount of data used to generate the results, the shape of the SPIRE estimate power spectrum is less than ideal. Improvements to the shape are discussed in Section 4.2.

For comparison purposes, the Minimum Variance (MV) [12] and MUSIC [14] algorithms were also used to process the results and the results are plotted in Figure 5b and c. A search grid employing the same $1° \times 1°$ spacing as used for the SPIRE algorithm, was also used by both the MV and MUSIC algorithms. Since MUSIC was originally developed for direction-of-arrival estimation, and not spectrum estimation, the square root of the MUSIC output has been displayed here and all other MUSIC plots in this report since this results in a better estimate of the relative spectral power levels.

The processing time for the example shown in Figure 5 was 38 seconds for basic SPIRE and 1.6 seconds each for MV and MUSIC. A faster method of producing the SPIRE results is discussed in the section 4.3.

4.2 Spatial Ambiguities

Given the large amount of data used to generate the data covariance matrix ($K = 10000$), a better correspondence might have been expected between the actual
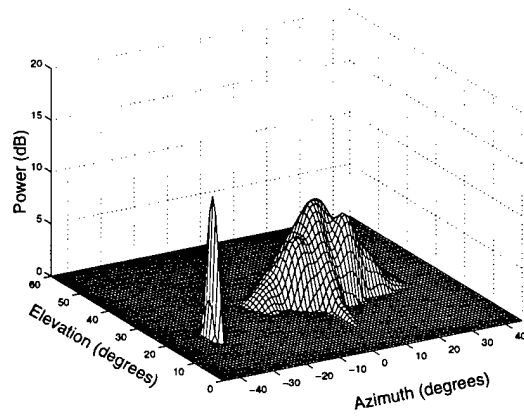
(a)
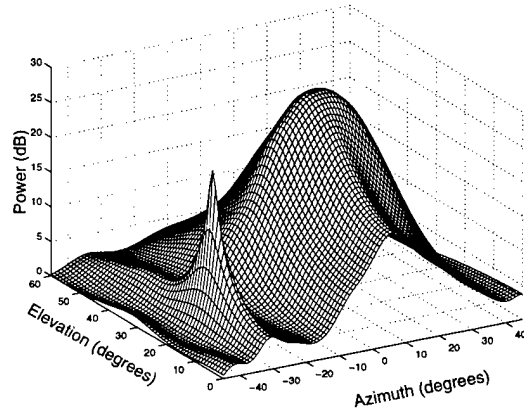
(b)
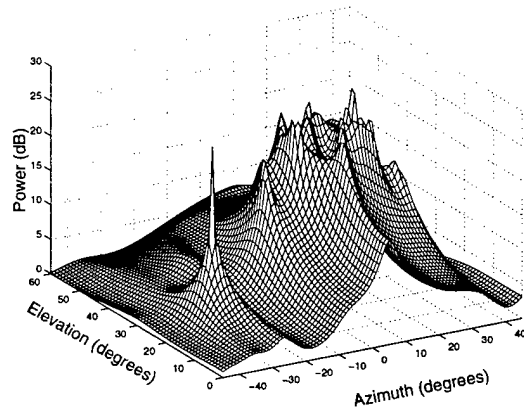
(c)

Figure 5: Results of processing $K = 10000$ samples of simulated data using: (a) basic SPIRE, (b) MV, and (c) MUSIC.

signal model shown in Figure 4 and the SPIRE estimated model shown in Figure 5a. However, the results illustrate an apparent ambiguity problem with the spatial power spectrum. For example, nearly identical results to those shown in Figure 5 can be produced with the signal model having the spatial power spectrum shown in Figure 6. In other words, the two signal models produce almost identical data covariance matrices although the spread-source signal regions have different spatial shapes.
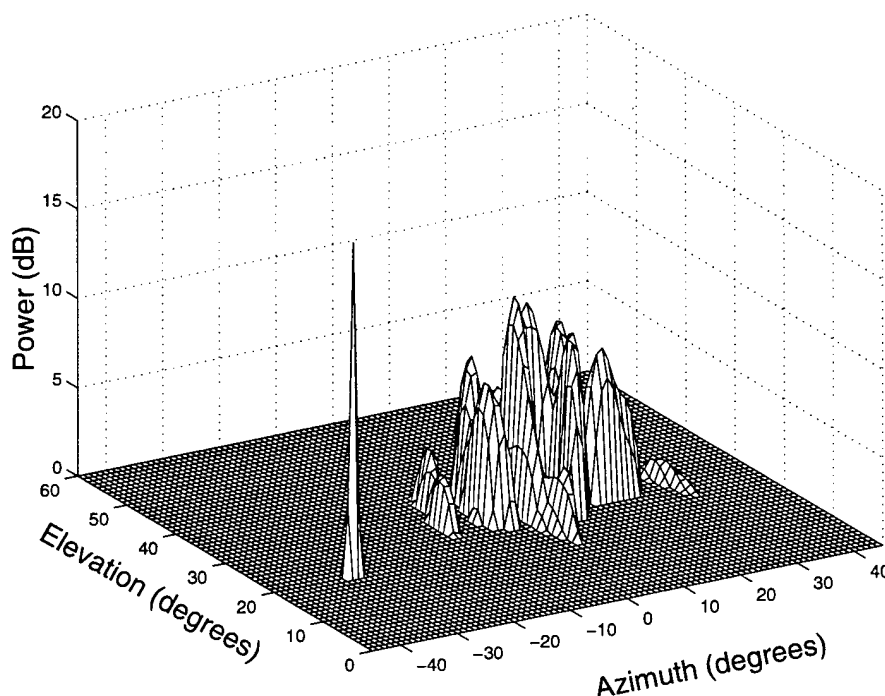
Figure 6: *Spatial power spectrum of alternate signal model which leads to virtually the same results as in Figure 5 when the model generated data is processed with basic SPIRE, MV, or MUSIC.*

This result is not totally unexpected since as smaller and smaller features are considered, the angular resolution limitations of the antenna array will become a problem. Hence, an arbitrarily shaped region will be indistinguishable from a point source, or any other arbitrarily shaped region for that matter, as long as the regions are very small and at the same angular position. Applying this idea to the features in Figures 4 and 6, "small" means less than the antenna array beamwidth.

Given this resolution problem, it makes more sense to estimate regions using the simplest shape that yields an acceptable solution rather than more complex shapes. Using this as a guideline, and investigating a number of different modifications to the basic SPIRE algorithm, the following modified algorithm was developed.

1. Perform basic SPIRE as outlined in Section 3 except using $max\_loop = 10$.

2. Subdivide the signal grid into P regions.

3. Do the following steps 4-12 twice.

4.   Initialize the region counter: $p = 0$.

5.   Increment the region counter: $p \rightarrow p + 1$.

6.   Select only grid signals from region p for further processing.

7.   Reduce all signal powers in region p by a factor of 2.

8.   Do steps 9-11 max_loop times.

9.   Include grid signals bordering region p.

10.   Update region m signal power estimates (Section 3.3).

11.   Remove any grid signals with zero power.

12.   While $p < P$ go to step 5.

After running the basic SPIRE algorithm, the signal grid will consist of mainly zero power signals with islands or regions of positive power signals. The first step in the modification, then, is to identify these regions. Once this is done, each region is separately processed using the basic SPIRE approach except that signal powers are initialized to half their previous value, and the regions are allowed to grow and shrink in size (steps 9 and 11).

Subdividing the grid into regions reduces the amount of processing since the "zero" parts of the signal grid are ignored. It also improves convergence. Halving the signal powers results in simpler spatial shapes. Steps 9 and 11 also allow the region to develop in a smooth manner.

Using this enhanced form of SPIRE for the same data used to produce Figure 5, the result is shown in Figure 7. Although not identical to Figure 4, the results are considerably improved compared to Figure 5 when the "simpler is better" guideline is followed.

An upper limit may also be imposed on the number of regions P to further reduce processing without significantly affecting the results *as long as P equals or exceeds the true number of spread-source signals.*

4.3 Signal Model Grid Spacing

The angular spacing between point-source signals used in the signal model grid must be sufficiently narrow for the model to represent a real spread-source signal adequately. However, making this spacing too narrow can unnecessarily increase the number of computations since the increase in computations is inversely proportional to the square
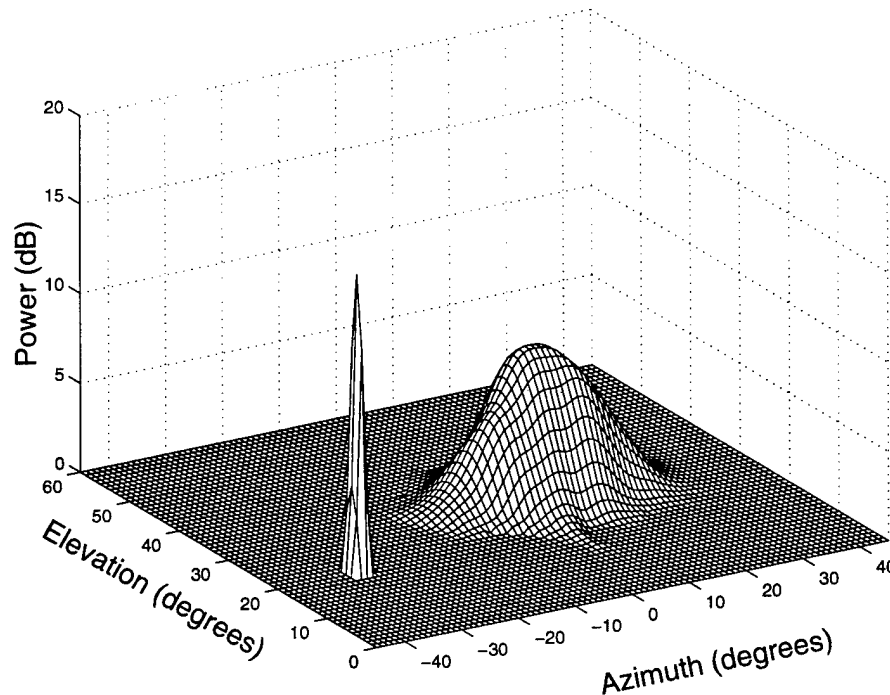
Figure 7: *Results of processing* $K = 10000$ *samples of simulated data using the enhanced form of SPIRE.*

of the spacing. Hence it is useful to determine the widest spacing that can be used before introducing too much error.

Since the resolving power of any antenna array is a function of the beamwidth of the array, a natural choice would be to use a spacing value which is some fraction of the minimum beamwidth of the array. Figure 8 shows several examples of the results of processing the same simulation example as before (see Figure 5f) where the signal model grid spacing was varied from 20% to 100% of the beamwidth (1.6° to 7.8°).

Comparing the different spacings, good results were obtained for spacings up to 80% of the beamwidth. At 80% or more, extraneous signals begin to appear in the results suggesting that this represents the upper limit on the spacing. A similar conclusion was also drawn in [3] for the SML algorithm based on an analysis of bearing accuracy versus grid spacing.

An advantage of the larger spacings is that since the processing time is inversely proportional to the square of the spacing, larger spacings means faster processing. A problem with larger spacings, however, is illustrated in Figure 9. In this example, two closely spaced point-source signals are detected but not resolved for spacings that are greater than half the angular distance between the signals (in this case 40% of the beamwidth or more). Hence one way to reduce the amount of processing, yet maintain acceptable resolution, would be to employ larger grid spacings for the early iterations
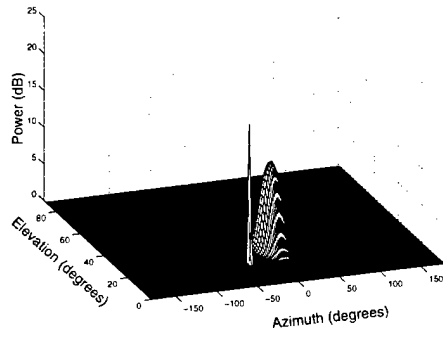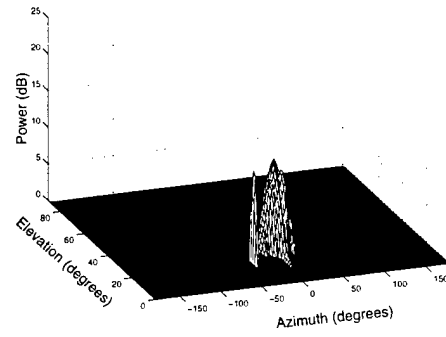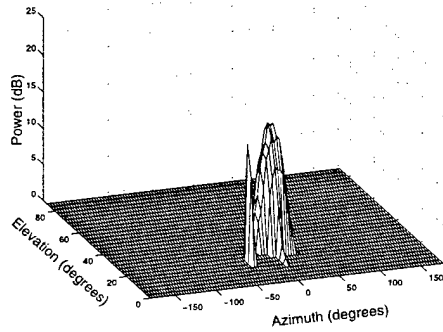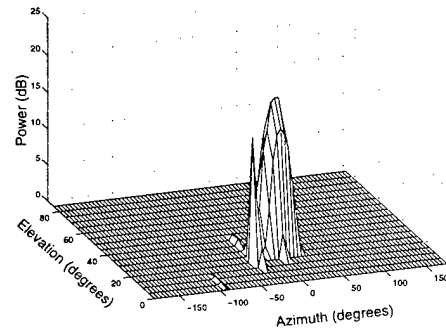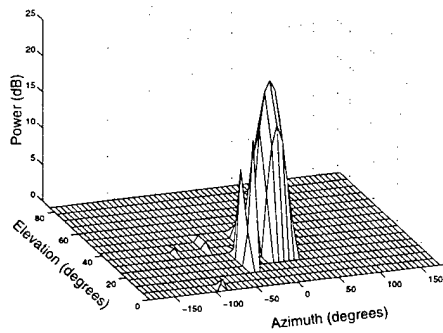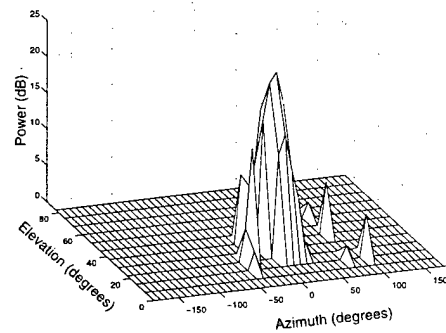
Figure 8: Results for SPIRE using various signal grid spacings showing (a) the simulation signal model, and the estimated models for spacings of (b) 20%, (c) 40%, (d) 60%, (e) 80%, and (f) 100% of the antenna array beamwidth.

and then finer spacings for the later iterations.
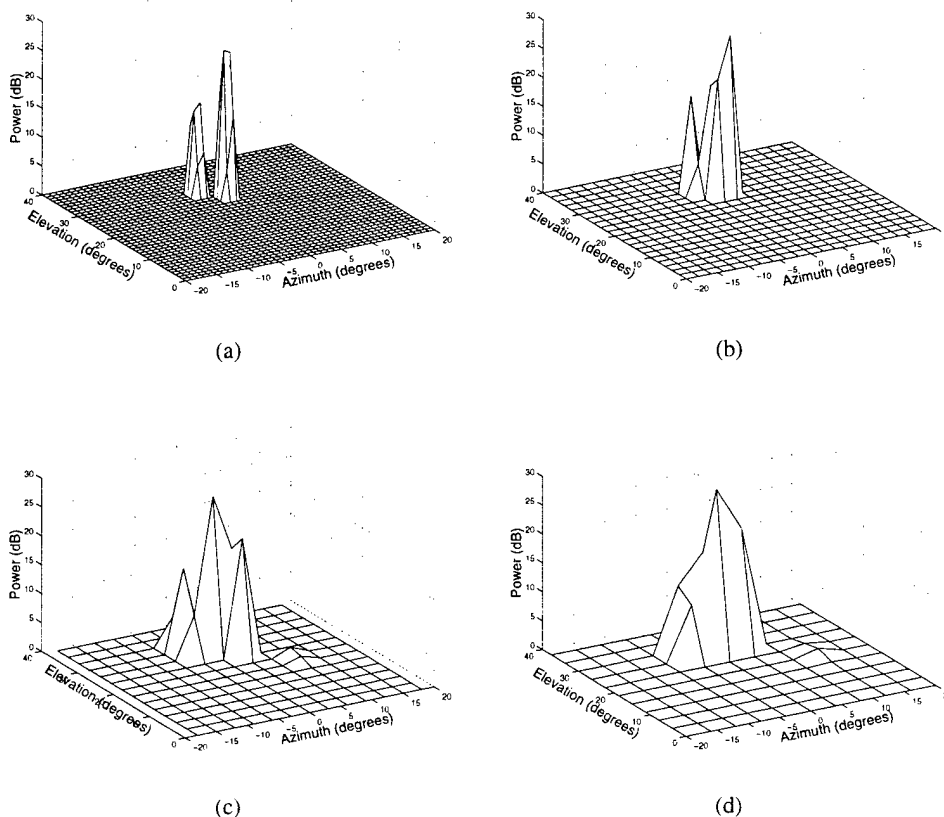
Figure 9: Resolution of two point-source signals with bearings $(\phi_1, \psi_1) = (-1.5°, 29°)$ and $(\phi_2, \psi_2) = (1.5°, 26°)$ and signal powers $s_1^2/\sigma^2 = 20$ dB and $s_2^2/\sigma^2 = 30$ dB. The SPIRE signal grid spacings used were (a) 1°, (b) 2°, (c) 3°, and (d) 4°.

Applying this coarse/fine spacing idea to the SPIRE algorithm, a fast version has been developed. Using the spacing scheme illustrated in Figure 10, the first 10 iterations are carried out using the coarse grid in the same manner as before but without the final noise power update. The signal power estimates are then interpolated from the coarse grid to the fine grid using a simple quadratic function. For example, all the signal powers of the coarse grid shown in the dotted box in Figure 10 are used to interpolate the fine grid signal powers within the solid box based on the expression

(46)
$$s = c_0 + c_1 x + c_2 y + c_3 xy + c_4 x^2 + c_5 y^2$$

where $x, y = \{-1, 0, 1\}$ are the Cartesian coordinates of the signals in the solid box (the spacing between adjacent fine grid signals is 1 unit and the center of the box represents the origin). The coefficients $c_0, ..., c_5$ are determined using least squares

estimation techniques in conjunction with the known coarse grid signal powers and $x, y = \{-3, 0, 3\}$. The coefficients are then divided by 9 to maintain the same signal power density since the fine grid contains 9 times as many model signals. The coefficients are further divided by a factor of 2 which causes an underestimate of s in (46), but ultimately results in a smoother transition from the coarse to the fine grid signal power estimate.
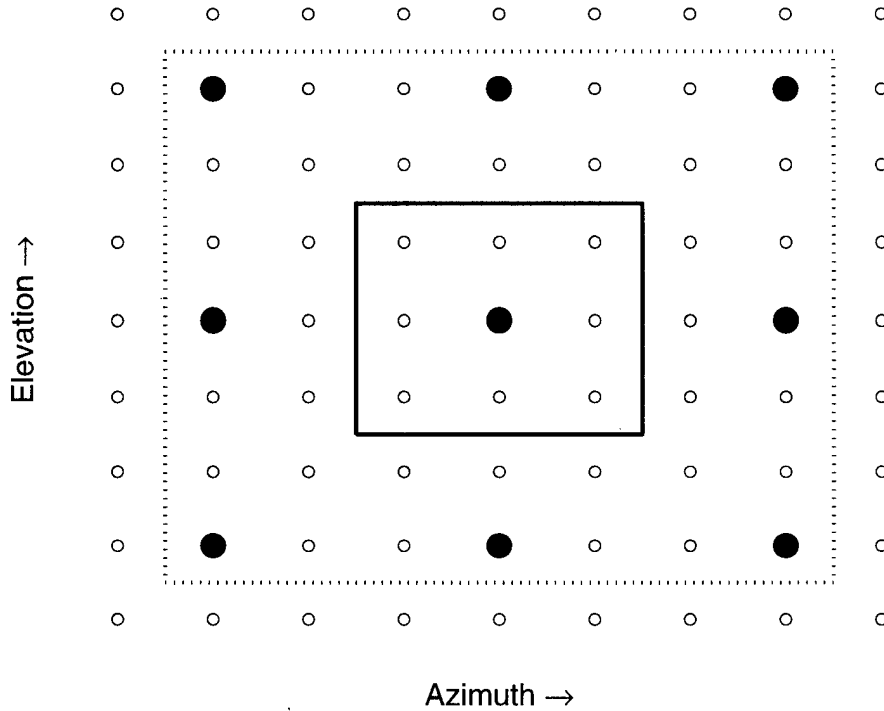
Figure 10: *Grid layout for coarse/fine processing scheme. The large dots represent the positions of the point-source signals used for initial (coarse) processing and the small circles plus large dots represent the positions used for final (fine) processing. The coarse grid signals within the dotted box are used to interpolate the fine grid values within the solid box.*

Using the pared fine grid, ten more iterations are then carried out followed by the final update of the noise power.

Along with the coarse/fine processing scheme, a further reduction in the amount of processing can be achieved by only updating signals in the fine grid which either have positive (nonzero) powers or border signals that have positive power. Since signals will usually be limited to small regions of the sky, the reduction in processing can be substantial. For example, using a 3° coarse spacing and 1° coarse spacing for the signal model grid, the computation time needed to produce Figure 5a was reduced by a factor of almost 8 (5.0 seconds versus 37.9 seconds).

Using the coarse/fine scheme for the enhanced form of SPIRE discussed in Section 4.2,

instead of the basic form, producing Figure 5f resulted in a reduction in the computation time of a factor of slightly more than 3 (11.2 seconds versus 37.9 seconds). The smaller improvement in this case was due to the fact that a portion of the computation time was taken up by extra processing stage which is the same whether the fast or basic version of SPIRE is used.

No doubt variable spacing schemes could be successfully employed to reduce processing further (e.g., spacing as a function of beamwidth and/or spherical distances between grid points), but this avenue was not investigated. Additionally, since the computations of the signal powers can be performed in parallel, much faster versions of the SPIRE algorithms could be implemented using parallel processors.

4.4 Data Sample Size

As stated previously, the key assumption in the development of the SPIRE algorithm is that all signals are uncorrelated with each other including signals from different parts of the same spread region. Consequently for collection purposes, a sufficient number of data samples must be collected to ensure that proper decorrelation occurs in the sample data.

To investigate the effect of the number of data samples K, a series of simulations was carried out using the same signal model used previously (shown in Figure 4), but varying the number of samples. The results are shown in Figure 11.

The results show that the spread region is most affected, becoming "hillier", as the number of samples decrease. This is a result of the sensitivity of the estimation process to the kinds of ambiguities discussed in Section 4.2. Small perturbations due to noise and incomplete decorrelation can have large effects on the estimated spatial shape of the spatial region. Since larger spread regions require a greater number of grid signals for modeling, there is a greater possibility for ambiguities. By way of comparison, a point-source signal only requires one grid signal with no possibility of any ambiguity. For this particular set of results, the spread region is accurately modeled for $K \geq 1000$ while the point-source signal is accurately modeled for all values of K, although the estimated signal exhibits spreading in elevation at the smaller values.

A second series of simulations was carried out featuring the "H" shaped signal model shown in Figure 12. As before, the number of samples was varied. The effect of decreasing the number of samples in this case is similar to the previous example.

To illustrate the improved abilities of the SPIRE algorithm to estimate the spatial power spectrum versus MV or MUSIC, some comparative results are shown in Figure 13 for $K = 1000$. The MV and MUSIC results shown in Figure 13 e and f were enhanced by showing only the spectrum within 10 dB of the peak value. This 10 dB threshold was based on knowledge of the actual spatial power spectrum of the signal – knowledge which wouldn't normally be available in practical applications.
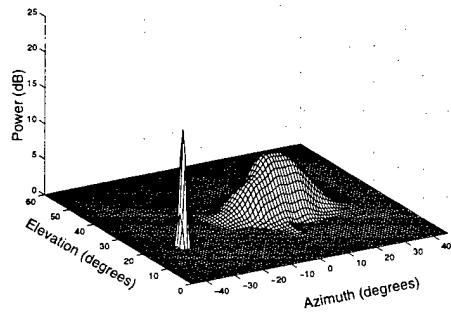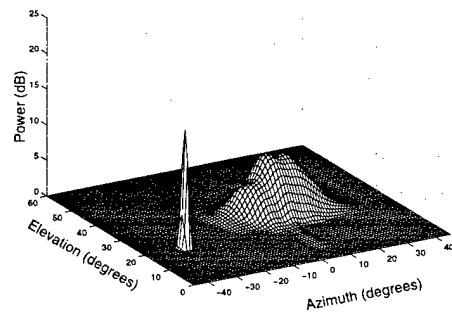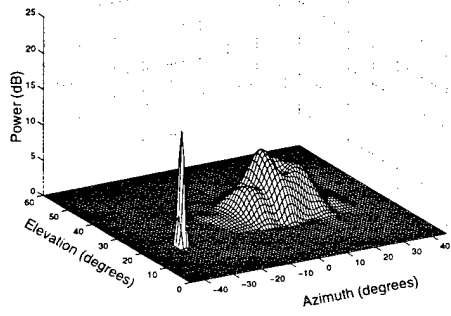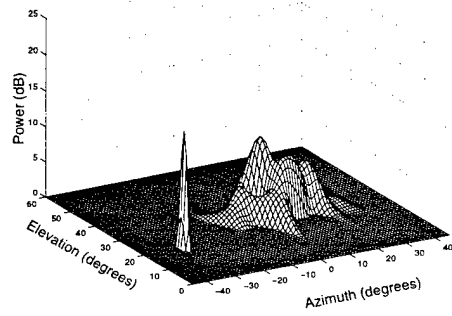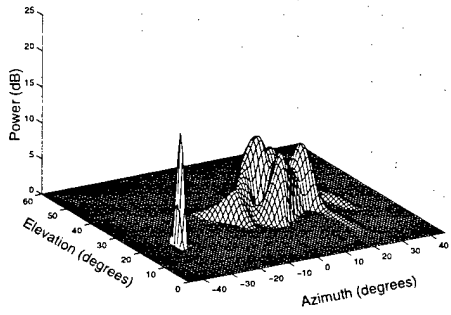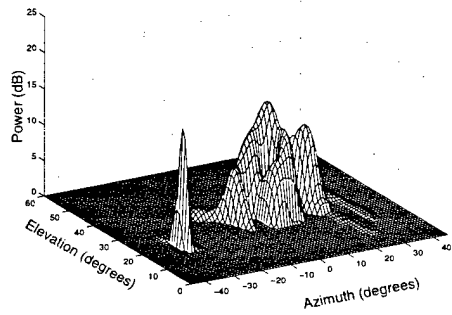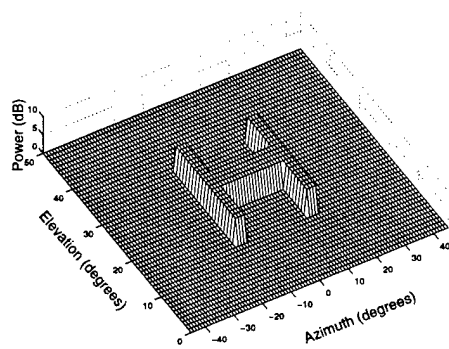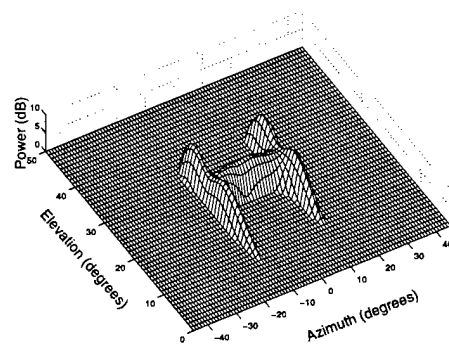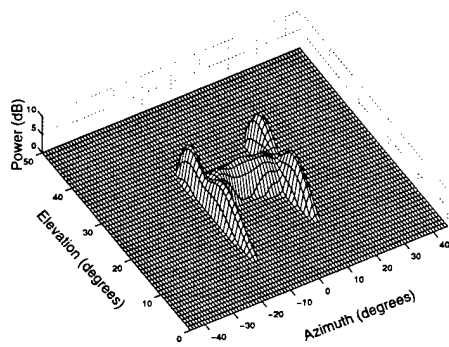
Figure 11: *The effect of varying the number of data samples on the performance of SPIRE. The results shown are for (a) $K = 10000$, (b) $K = 1000$, (c) $K = 300$, (d) $K = 100$, (e) $K = 50$, and (f) $K = 25$.*
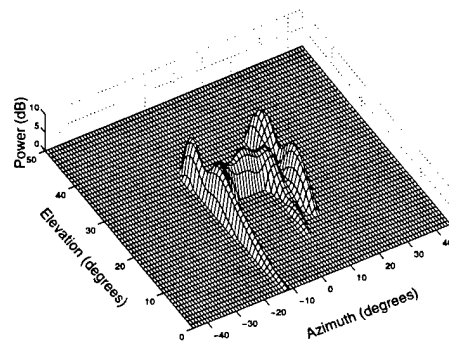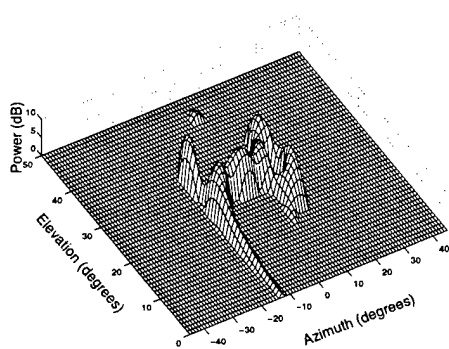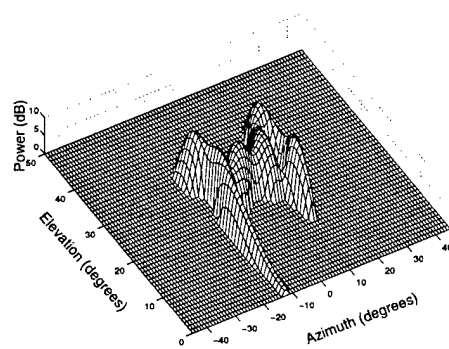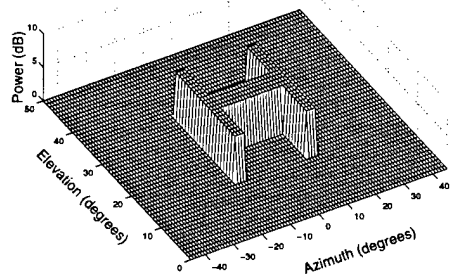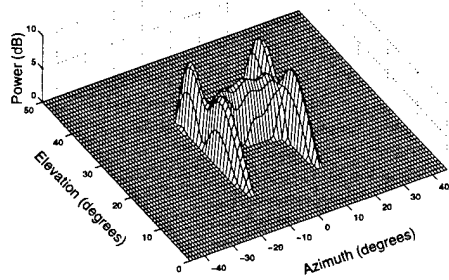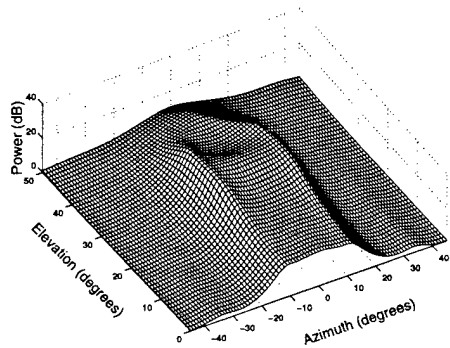
Figure 12: *The effect of varying the number of data samples on the performance of SPIRE for a signal with the "H" shaped spatial power profile shown in (a). The SPIRE results shown are for (b)* $K = 1000$, *(c)* $K = 300$, *(d)* $K = 100$, *(e)* $K = 50$, *and (f)* $K = 25$.
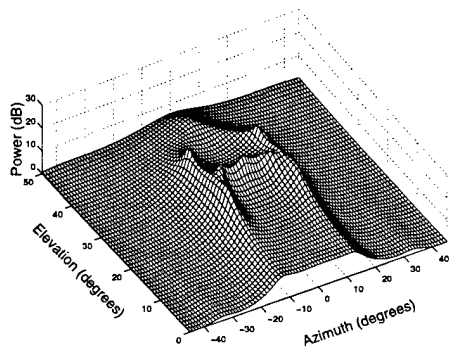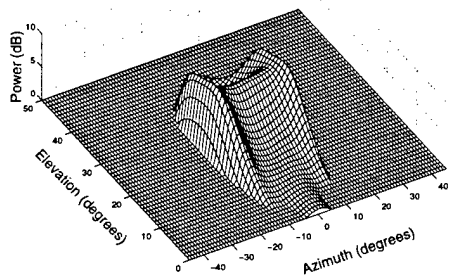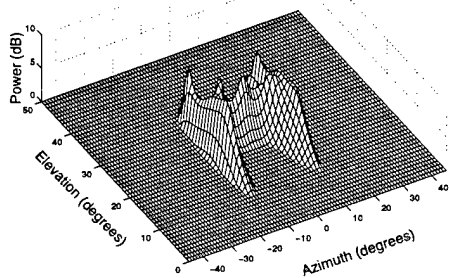
Figure 13: *A comparison of the estimation accuracy of SPIRE, MV, and MUSIC for the "H" shaped signal using* $K = 1000$ *and showing (a) the true signal spatial power spectrum, (b) the SPIRE result, (c) the MV result, (d) the MUSIC result, (e) the modified MV result, and (f) the modified MUSIC result. For the modified results, only features within 10 dB of the maximum peak value are shown.*

Finally, the effect of sample size on the measured model error ε is shown in Figure 14. The plotted model error is the average of the error values generated when processing the simulated data used to produce Figure 11 (the spread-source and point-source signals) and Figure 12 (the "H"-shaped signal). The results show that the "H"-shaped signal was easier to model than the spread-source signal plus point-source signal. The reasons are likely due to the ambiguity problem discussed earlier (the wider angular area of the spread-source signal would suffer the ambiguity problem more than the narrow ridges of the "H"-shaped signal), and the quantization effect (the point-source can only be exactly modeled if its bearing corresponds with the bearing of a signal in the signal model grid).
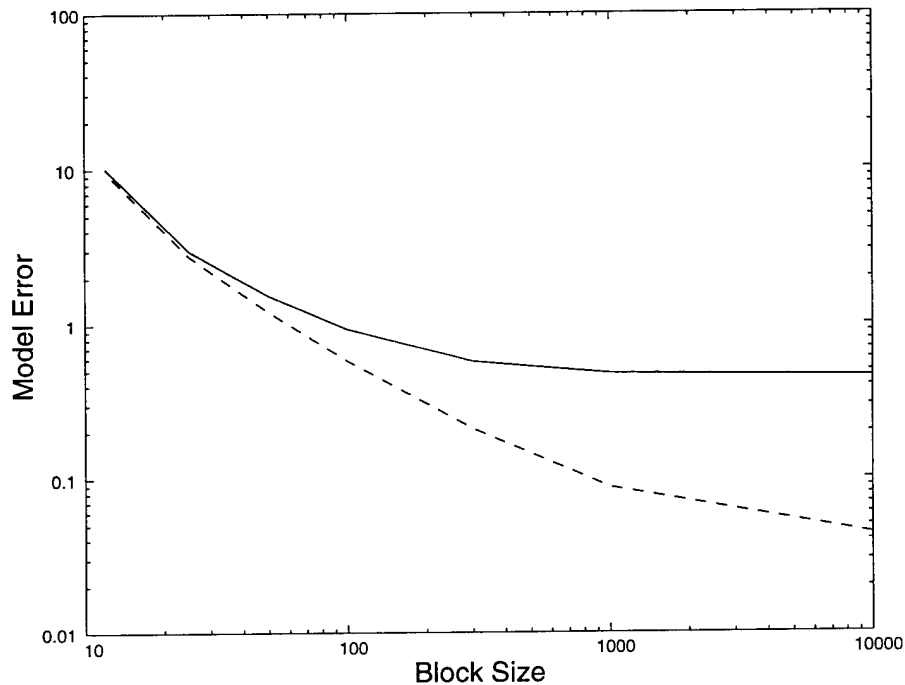

Figure 14: Model error as a function of sample size. The upper curve (solid line) shows the results for the same data used in Figure 11 (point-source and spread-source signals). The lower curve (dashed line) shows the results for the same data used in Figure 12 ("H"-shaped signal).

4.5 Number of Signals

The general rule used to determine the maximum number of signals that may be estimated using a superresolution algorithm is $N - 1$ where N is the number of sensors. This rule applies to algorithms which make no assumption about signal correlation (i.e. the correlations are implicitly or explicitly estimated).

The SPIRE algorithm assumes that the signals are fully uncorrelated so that estimation of the signal correlations is not required. As a result, the $N - 1$ limit can be exceeded as illustrated in Figure 15 where the bearings of 13 uncorrelated point-source signals

(Figure15a and b) are correctly estimated using an array of 12 antennas (Figure15c and d). A few spurious signals were also estimated with the maximum false peak in the spectrum still 5 dB below the minimum true signal peak.

The MV algorithm also has the capability to exceed the $N - 1$ limit as illustrated in Figure 15e and f where the 13 largest peaks correspond to the true signals. However, the resultant spectrum is considerably more difficult to interpret than the SPIRE spectrum with many more false peaks, and with some of them coming within 1 dB of a true peak.

The MUSIC algorithm is limited to $N - 1$ signals and consequently no results are shown here.

Although the results suggest that there is no hard upper limit for uncorrelated signals, they illustrate that estimating an increasing number of signal directions comes at the price of lower accuracy. The SPIRE algorithm was able to estimate all 13 signals in the example, but the results are not as good as the results shown in Figure 9a or Figure 11b where only two signals were involved. From the practical point-of-view, it seems more reasonable to use the SPIRE algorithm for environments where the number of signals is somewhat less than the number of sensors.
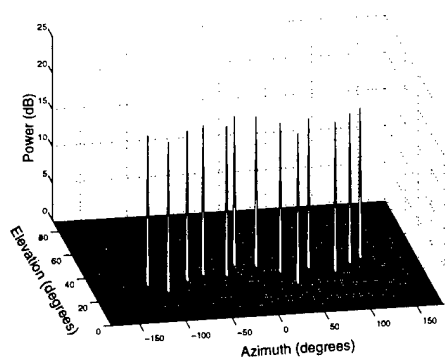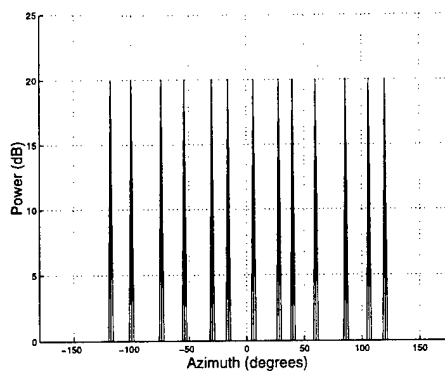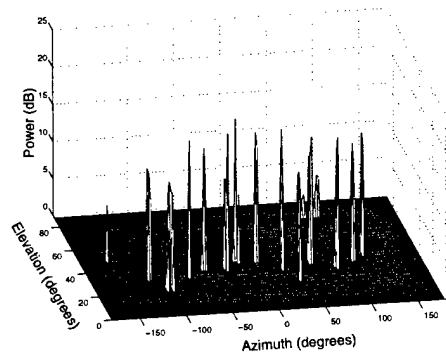
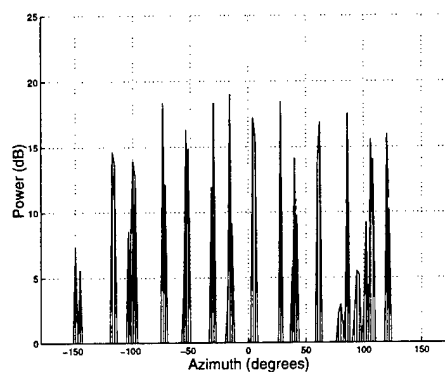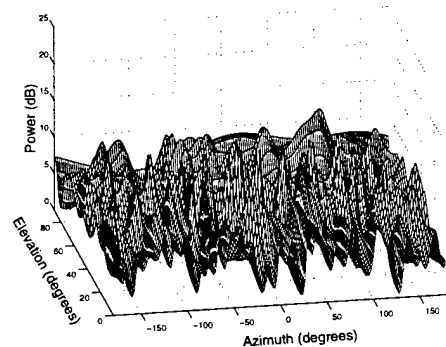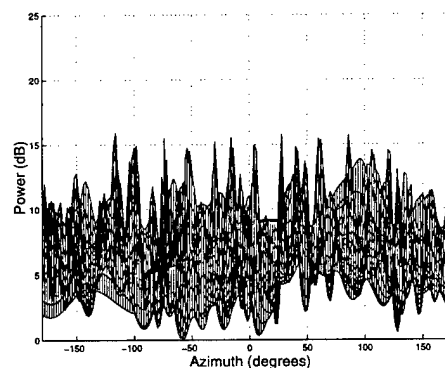**Figure 15:** *An example of estimation of 13 point-source signals using 12 antennas, $K = 1000$, and SNR = 20 dB, showing (a) the actual spatial signal spectrum, and (b) azimuth profile,(c) the spectrum estimated using enhanced SPIRE and (d) azimuth profile, and (e) the spectrum estimated using MV and (f) azimuth profile.*

5. SPIRE PERFORMANCE

The previous section dealt with computational issues relating to the SPIRE algorithm. In this section, the effect of various uncontrolled parameters on the performance of the SPIRE algorithm is studied. These parameters are discussed in the next few sections and include SNR, signal spreading, and angular spacing between signals. Where appropriate, the results using the MV and MUSIC DF algorithms are also shown for comparison purposes.

Since the SPIRE algorithm is designed to estimate the direction of signal power regardless of the spatial spreading of the signal source (unlike other algorithms such as MUSIC and MV which assume point sources only), the peaks in the estimated spatial spectrum do not necessarily yield the true direction of spread-source signals; particularly when the ambiguity problem is taken into account (consider Figure 11f for example). A more appropriate method is to take the power weighted average of all the grid signals associated with a given region. For example

$$(47) \qquad \hat{\phi}_k = \frac{1}{M_k} \sum_{i=1}^{M_k} s_{ik} \phi_{ik}$$

$$(48) \qquad \hat{\psi}_k = \frac{1}{M_k} \sum_{i=1}^{M_k} s_{ik} \psi_{ik}$$

where $\hat{\phi}_k$ and $\hat{\psi}_k$ are the azimuth and elevation bearing estimates of the kth signal region, M_k is the number of grid signals required to model the region, s_{ik} is the signal power of the ith grid signal in the kth signal region, and ϕ_{ik} and ψ_{ik} are the associated azimuth and elevation bearings of the same grid signal.

Although no research has been done to determine whether the above bearing estimation method is optimum, for simulation testing it was found to yield results which were better than those obtained when using the spectral peaks.

Signal power was estimated as the sum of the grid signals in the associated region, that is

$$(49) \qquad \hat{\rho}_k = \sum_{i=1}^{M_k} s_{ik}$$

where ρ_k is the signal power.

In this section, and throughout the rest of this report, the grid size used for the SPIRE model was $1° \times 1°$, unless otherwise specified.

For assessment purposes, the processed results were quantified in two ways. The first was the measurement of the failure rate of signal bearing estimates, and the second was the measurement of the accuracy of the successful estimates. A bearing estimate was considered to be a failure if it deviated from the true signal bearing by more than half

the array beamwidth (taking into account both the azimuth and elevation beamwidths). Accuracy was determined by calculating the root-mean-squared (RMS) error of the estimates according to

$$(50) \qquad RMS\,Error = \sqrt{\frac{1}{H}\sum(\hat{\phi}_m - \phi_m)^2 + (\hat{\psi}_m - \psi_m)^2}$$

where the summation was performed for all H successful estimates of signal m.

5.1 Effect of Noise

The effect of noise was investigated through simulation. In the first series of simulations, a single point-source signal at $(\phi, \psi) = (180°, 30°)$ was generated and the SNR was varied from -20 dB to +40 dB in 2 dB increments. One hundred trials were repeated for each SNR setting. In the second series of simulations, the point-source signal was changed to a spread-source signal with spread parameters $(\Delta_\phi, \Delta_\psi) = (30°, 15°)$, but all other parameters remained the same. The results after processing the data with the SPIRE algorithm are shown in Figure 16. For comparative purposes the results using the SML algorithm are also shown.

Several features of the results are worth pointing out. The SNR at which the failure rate dramatically departs from 0% is called the threshold SNR. For the point-source this occurs between -12 and -10 dB and for the spread-source, it is worse, occurring about -6 dB for the SPIRE algorithm and -8 dB for the SML algorithm. The poorer performance for the spread-source signal (including both threshold and accuracy) compared to the point-source signal is a function of the amount of spreading.

The effect of signal spreading on accuracy can be attributed to two factors: signal model uncertainty and the filter effect (see also [1]). The first factor, signal model uncertainty, arises from the fact that the spatial model for the spread-source signals is stochastic and requires a sufficient number of snapshots to build up the appropriate statistics in the data as was discussed in Section 4.4. For a single point-source signal, a single snapshot is sufficient. For a spread-source, the number of snapshots required to achieve a given accuracy rises as the spread region increases in size. Conversely, for a given number of snapshots, accuracy degrades as the spread region increases.

The second factor, the filter effect, can be understood by considering that many advanced DF algorithms, such as MV, MUSIC, SML, and SPIRE, can be interpreted as techniques which work by designing spatial filters to reject the signal content of the data. Point-source signals are matched by very narrow notch filters while spread-source signals are matched by appropriately shaped band rejection filters. The greater the amount of noise rejected by the filter, the greater the effect on the estimation error since the idea is to reject the signal but pass the noise. Hence estimation accuracy degrades as the spread region increases.
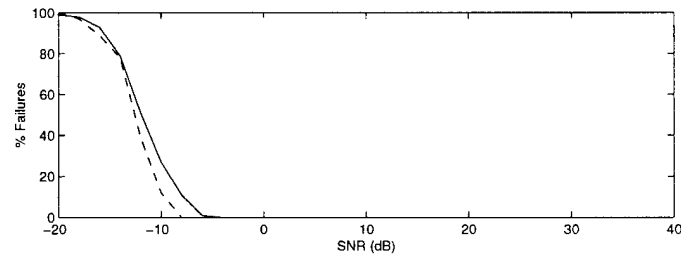
The scales used to display the RMS bearing errors in Figure 16(b) were chosen because they linearize the accuracy results for the point-source signal above the threshold SNR.
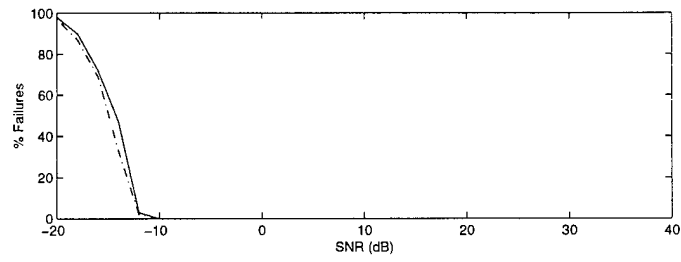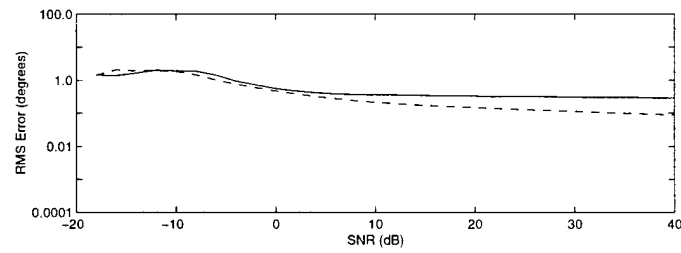
(a)
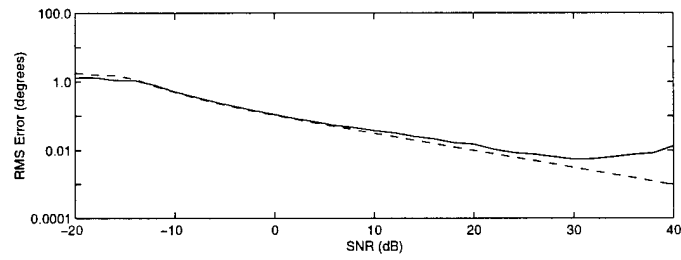
(b)

(c)

(d)

Figure 16: *Effect of the signal-to-noise level on estimation performance of the SPIRE (solid lines) and SML (dashed lines) algorithms showing (a) the failure rate and (b) accuracy of the point-source, and (c) the failure rate and (d) accuracy of the spread-source signal.*

In this region, for every 20 dB increase in SNR the RMS bearing error is reduced by a factor of 10. Written mathematically, the relationship is expressed as

$$\epsilon \propto \sqrt{SNR} \qquad (51)$$

where ϵ is the RMS bearing error. The spread-source also exhibits the same behaviour between -8 and 0 dB, but above this SNR the error begins to level out as the uncertainty in the signal model begins to dominate the error (as discussed previously in Section 4.4). At higher SNR's, the only way to improve accuracy would be to use a larger sample size.

Comparatively speaking, the performance of the SPIRE algorithm is worse than the SML algorithm. For the point-source signal, the failure rate was the same for both signals as was the accuracy for an SNR less than 10 dB. For an SNR between 10 dB and 30 dB, the RMS bearing error was about 1.4 times greater for the SPIRE algorithm than the SML algorithm. Above 30 dB, the increase in the RMS error for the SPIRE algorithm is due to the signal model grid spacing chosen ($1° \times 1°$). For a smaller grid spacing (i.e. $0.5° \times 0.5°$), the SPIRE error reduces from 12 times to 1.4 times the SML error.

For the spread-source signal, the SPIRE algorithm again produces less accurate results with RMS errors up to 3 times that of the SML algorithm.

Although the poorer performance of the SPIRE algorithm might at first seem disappointing, it is a consequence of the greater adaptability of the SPIRE signal model. The SML algorithm assumes a fixed shape and power density for each signal's spatial profile. In these examples, this profile was identical to what was actually simulated giving the SML algorithm an advantage. In the real world, this would not be true in many situations giving the SPIRE algorithm an advantage since it is able to adapt to the conditions.

Note that when used to process the same data, the MUSIC and MV algorithms produced the same results as the SML algorithm for the point-source signal, but were about $20\times$ worse for the spread-source signal.

The last set of results displayed for the noise simulations is the effect of signal-to-noise ratio on the model error which is shown in Figure 17. Comparing the two signals, model error for the spread-source is relatively independent of the noise level, while the model error for the point-source increases with decreasing noise level. This is due to the fact that the point-source cannot be perfectly modeled unless a signal in the model grid is exactly aligned in bearing with the actual signal (in the simulations, the nearest grid signal was misaligned from the actual signal by $0.5°$ in both azimuth and elevation). As the SNR is increased, the contribution of the noise component decreases making the modeling mismatch in the signal component more pronounced. This error could be reduced by decreasing the grid size.
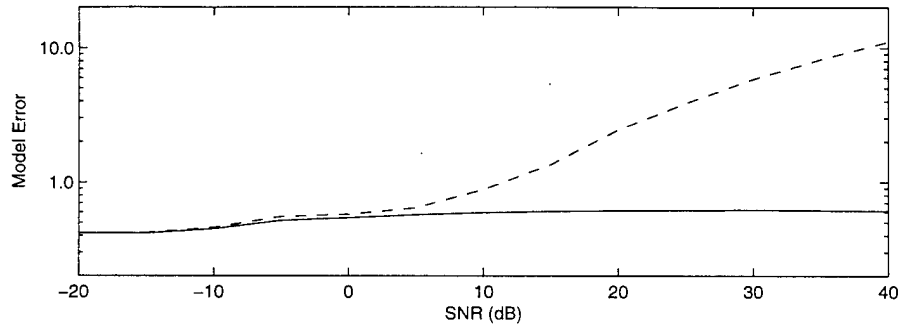
Figure 17: *The effect of noise on model error. The solid line shows the results for the spread-source signal and the dashed lines shows the results for the point-source signal.*

5.2 Detection of a Weaker Signal

One important test of a DF estimator designed for high latitude HF operation is the ability to detect a weaker point-source signal in the presence of stronger spread-source signals. To evaluate the performance of the SPIRE algorithm, simulations were run involving a single spread-source with a fixed bearing and a single point-source whose bearing was adjusted incrementally, beginning with a large initial angular difference, until the two bearings coincided. After each increment, the signal power of the point-source was increased from a low value in 0.5 dB intervals until the failure rate dropped below 5% (5 out of 100 trials). The corresponding SNR of the point-source signal is defined here as the threshold SNR and provides a good indication of the limits of detectability of the point-source signal for the given signal environment. The relevant signal and noise parameters are shown in Table 1.

Table 1: *Signal Parameters for Signal Detectability Simulation*

Signal	ϕ	ψ	Δ_ϕ	Δ_ψ	Power
1	180°	30°	30°	15°	0 dB
2	adjusted	30°	0°	0°	adjusted
noise	–	–	–	–	-20 dB

One practical difficulty with the SPIRE algorithm is that as the separation between the two sources becomes smaller and smaller, the regions begin to merge so that one region describes two sources. For the sake of these simulations, when the regions had merged, the peak in the combined region most closely corresponding to the weak signal was used to determine the bearing estimate of the weak signal. This was considered reasonable for separations of 15° to 10°, since the weaker signal was clearly identifiable when examining the spatial spectrum. At small angular separations, however, no attempt was made since separating the peak of the weaker signal from the peaks associated with the stronger signal was essentially a hopeless task.

The results from the simulations are shown in Figure 18. In this case, the failure rate is not shown since it was fixed to approximately 5%. From the results it is clear that when the point-source and spread-source signals are well separated, 25° or more ($> 1.2\phi_{BW}$), the presence of the spread-source signal has a small but significant effect. For example, the threshold SNR for a point-source without any other signals present occurs at -12 dB (see Figure 16). In the presence of the spread-source, the threshold SNR ranges from -10 to -8 dB, a degradation of 2 to 4 dB. As the separation between signals is reduced from 25° to 10°, the threshold SNR increases dramatically to 8 dB which is 20 dB higher than when no spread-source is present.

The differences between the wide and narrow separation cases can be understood in terms of using a spatial filter to suppress the effects of the spread-source signal. In the wide separation case, the filtering can be accomplished easily, leaving only the noise as the main source of error. In the narrow separation case, it is more and more difficult to filter out the spread-source signal independently of the point-source signal as the separation decreases. Consequently, the spread-source signal begins to act as a strong noise background and the threshold increases accordingly.

The accuracy results for the two signals are relatively constant for wide spacing and relatively independent of the presence of each other. For example, in the single signal case, the accuracies were measured to be 0.33° for the spread-source signal (20 dB SNR) and no point source signal, and 0.7° for the point-source signal (-12 dB SNR) and no spread-source signal – worse for the point-source signal due to the much lower SNR. For narrower spacings, the threshold signal power of the point-source signal increases, degrading the accuracy of the spread-source signal until the separation becomes as small as 8°. The accuracy of the point-source remains in the range of 0.5° − 1.5° for most separation angles with the largest errors occurring for the smaller separations.

The simulations were also repeated using both the SML and MUSIC algorithms. The assumed number of signal directions for the SML algorithm was two. For the MUSIC algorithms, six directions were assumed, since occasionally up to five directions were required to describe the spread-source leaving at least one direction for the point-source. In most cases, however, only three or four signal directions were required for the spread-source signal, resulting in one or more false direction estimates.

Generally, the necessity of using several signal directions to describe a spread-source signal and the problem of extraneous signals, makes the interpretation of the MUSIC results somewhat problematic. For the sake of this report, only the two (out of six) estimated signal bearings closest to the true signal bearings were used when generating the statistical results. Additionally, since for separation angles less than 10° there was no obvious way to determine whether a peak was associated with the spread-source signal or the point-source signal (like the SPIRE algorithm), no statistical results were calculated for these angular separations.
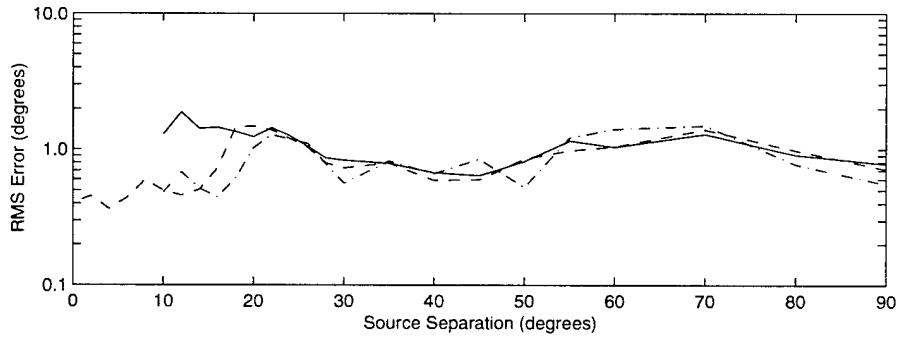
The failure and accuracy results for SML are shown by the dashed lines in Figure 18, and the corresponding results for MUSIC are shown by the dash-dot lines.
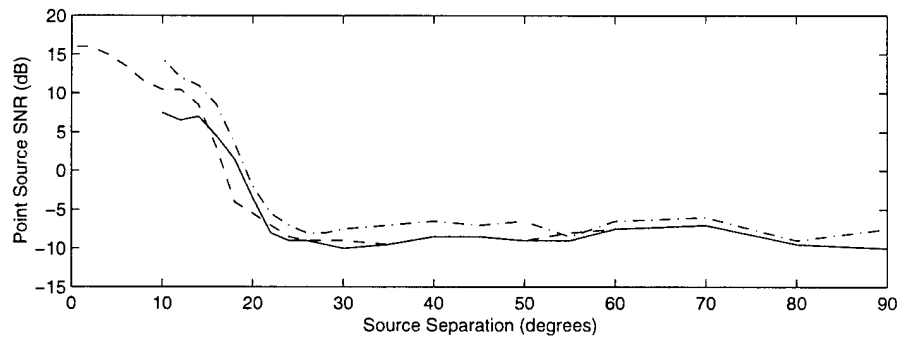
(a)
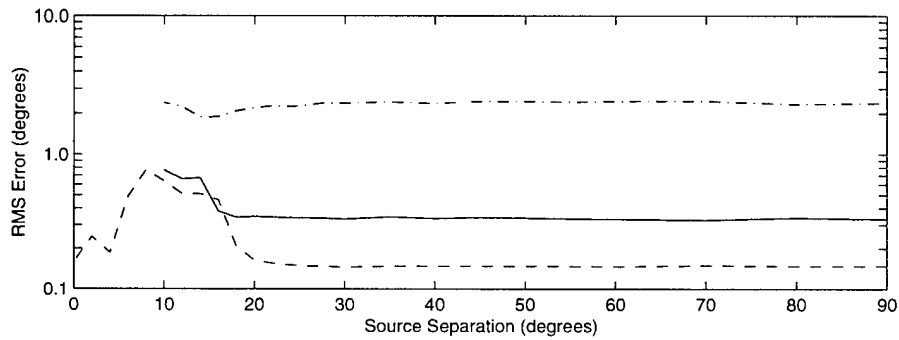
(b)

(c)

Figure 18: *Effect of angular spacing on the ability to detect a weaker point-source signal in the presence of a stronger spread-source signal showing (a) the detection threshold SNR for the weaker point-source signal, (b) accuracy of the spread-source estimates at threshold, and (c) accuracy of the point-source estimates at threshold. The solid lines represent the SPIRE results, the dashed lines represent the SML results, and the dash-dot lines represent the MUSIC results.*
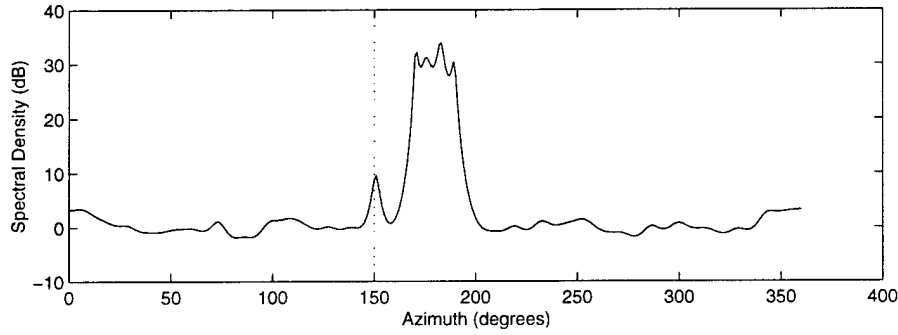
(a)
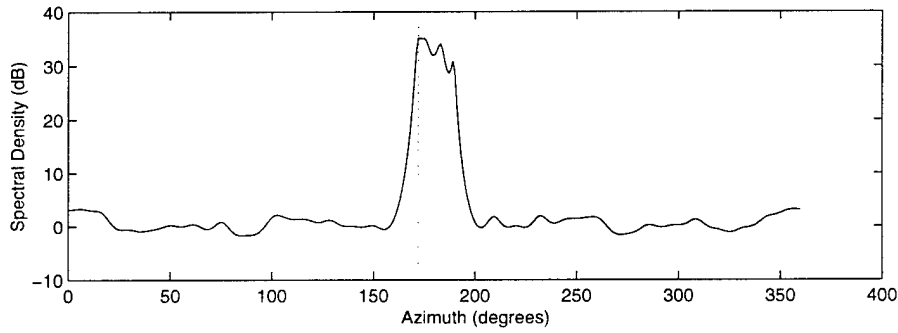
(b)

Figure 19: Detection of a weaker point-source signal in the presence of a stronger spread-source signal using MUSIC. The azimuth spectrum is shown for an elevation angle of $\psi = 30°$. The simulation parameters for the noise and spread-source are listed in Table 1, and the point-source parameters were (a) $\phi = 150°$ with a signal power of -7.5 dB and (b) $\phi = 172°$ with a signal power of 14.5 dB. When the separation between the spread-source and point-source is too narrow, as in (b), there is confusion as to which spectral peak belongs to which signal.

The results show that over the range of separation angles tested, SPIRE is able to detect signals 2.5 dB weaker than MUSIC. Compared to SML, performance is the same for separations greater than 20°, but generally worse for smaller separations. Below 10°, the SML algorithm is the only algorithm capable of separating the two sources.

The accuracy in estimating the point-source signal direction was the same for all three algorithms. However, since the SML and SPIRE algorithms had lower thresholds, this implies that tested at the same SNR (e.g., the MUSIC threshold) the SML and SPIRE algorithms are more accurate than MUSIC. The accuracy of MUSIC for estimating the direction of the spread-source signal was very poor, highlighting the difficulty of estimating spread-source signals using a point-source model. The accuracy of the SPIRE algorithm was poorer than the SML algorithm, indicating that some degradation occurs when the shape of the signal's spatial power spectrum is not known a priori.

Generally the results show that for signal environments with spread-source signals, improved modeling leads to significantly better performance.

6. PERFORMANCE USING HIGH LATITUDE OFF-AIR DATA

The ultimate test for any algorithm is against the actual data for which the algorithm was designed. In the following sections, an analysis of the SPIRE algorithm is carried out using high latitude off-air HF data. This analysis also includes results from the MV and MUSIC algorithms.

In the comparative analysis of these algorithms, the SPIRE results appear to be worse than the MV algorithm. However, it was found that mutual coupling problems almost certainly affected the data measurements possibly making the results for the MV algorithm look better than they should have been. The diagnosis of this problem using the SPIRE error function, and subsequent discussion, is also included in the following analysis.

6.1 The Equipment

The measurement system used to collect the data was an experimental 12 channel receiver system, called "Vortex", located at CFB Alert on the northern tip of Ellesmere Island in Northern Canada (82.50° N, 62.35° W). The receiver system was connected to an antenna array which had the geometric configuration shown in Figure 20. The array utilized 8 elevated feed monopole antennas from the inner ring of a Pusher array (a circular array with 24 antennas) and 4 outlying antennas (also elevated feed monopole antennas) which were added to increase the array aperture.
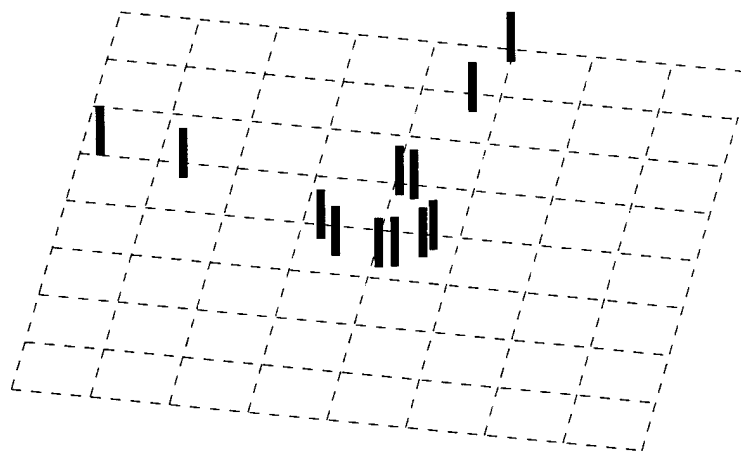
Figure 20: Three dimensional view of the Vortex antenna array. Each grid square has a dimension of $1\lambda \times 1\lambda$.

The Vortex receivers were used to downconvert the input signals from HF to 2.5 kHz with a filtered bandwidth of 3.5 kHz. The downconverted signals were then digitized at a rate of 10 kHz and the data stored for later processing.

6.2 Processing Considerations

To generate the covariance estimates, an FFT was performed on each sample block of 12×16000 data points and only the positive frequency data from 3.8 to 4.2 kHz was retained. This served the dual purpose of converting the data to IQ format and suppressing interference due to noise and other unintended HF signals. The data covariance matrix was then formed directly from 10 consecutive samples of this frequency domain data.

Although a value of $K = 10 \times 16000$ (representing 16 seconds) would appear to be sufficient based on the discussion in Section 4.4, this does not take into consideration the requirement for sample to sample decorrelation. The time required to achieve this decorrelation is related to the Doppler spreading of the signal, and can be approximated by $\tau = 1/(Doppler\ Spread)$. Using a Doppler spread value of 40 Hz (see discussion in Section 2.3), this gives a value of $\tau = 25$ ms. For 16 seconds of data, this corresponds to an effective sample size of $K = 640$. Since 40 Hz represented one of the larger values of Doppler spreading observed for the data discussed in [10], the effective sample size for the data discussed here may have been lower. For this reason, the 16 second choice for the sample size is analyzed in more detail in Section 6.5.1.

When processing the data using the SPIRE algorithm, it was found that the bearings of peaks in the estimated spatial spectrum were often noticeably different than bearings computed using the weighted region approach as defined in (47) and (48). This was due to the fact that the estimated signal regions were often asymmetric and sometimes contained multiple peaks. In some cases, it also appeared that the peak derived bearings were more accurate than the weighted region bearings. Consequently, peak derived bearings were also included in the analysis.

To overcome the problem of quantization for the peak derived bearings (since peak locations were restricted to bearings of the signal model grid), more accurate bearings were interpolated by fitting a Gaussian shape to the grid peak and its immediate neighbouring points. The peak of the fitted Gaussian function was then used as the improved bearing estimate.

To denote the difference between the SPIRE bearing estimates determined using the weighted region approach and bearing estimates determined using the peaks approach, the former are termed "region bearings" while the latter are termed "signal bearings" throughout the rest of this report.

For processing using the MUSIC algorithm, the 'number of signals' parameter was calculated using the Akaike Information Criterion as described in [17].

Both the MUSIC and MV algorithms were adapted to use the measured noise covariance C_η by modifying the steering vector and data covariance according to

$$(52) \qquad e \rightarrow \frac{C_\eta^{-\frac{1}{2}} e}{\| C_\eta^{-\frac{1}{2}} e \|}$$

$$(53) \qquad R \rightarrow C_\eta^{-\frac{1}{2}} R C_\eta^{-\frac{1}{2}}$$

where C_η was the measured noise covariance matrix.

The noise covariance C_η was determined in the same way as the signal covariance matrix except all the positive frequency data in the passband was retained except the signal portion from 3.8 to 4 kHz. The measurements over a period of approximately 20 minutes were then averaged to ensure a stable estimate

6.3 The Data

Two data sets were chosen for this discussion. Both collections were of signals originating from the CFH transmitter located in Halifax, Nova Scotia, Canada. The great circle signal bearing of the transmitter was 181.9°. The received signal was collected at a frequency of 10.9445 MHz.

The first data set was collected on September 2, 1995 from 13:25:28 to 17:40:12 UT during the Arctic daytime. The second data set was collected on January 24, 1996 from 21:01:92 to 23:32:12 during the Arctic night (which lasts 24 hours a day at that time of year).

Of the two signal periods, the first represents a time when benign signal propagation conditions would normally be expected (daytime) while the second represents a time when disturbed conditions might be expected [18]. This is, in fact, what was observed.

6.4 DF Results

The DF results for the two data sets, with the three different algorithms, are shown in Figures 21 and 22. Additional results are also shown for the SPIRE algorithm in Figures 23 and 24, including region bearing estimates and power, for both data sets. For the SPIRE region estimates, results were discarded if the corresponding region power was less than 0 dB.

For the September 1995 data, the results in Figure 21 and Figure 23 show that the MV algorithm produced the most accurate results and the SPIRE algorithm produced the worst – the exact opposite from what was expected.

The two signal bearings estimated by the SPIRE algorithm in Figure 21a and b, are peaks from the same region so that the scatter in the estimates is a reflection of the width of the corresponding region, i.e., tens of degrees of in both azimuth and elevation.

The large amount of signal spreading explains the poorer performance of the MUSIC algorithm compared to the MV algorithm. MUSIC's superior resolving power for point-source signals works against it when dealing with spread-source signals. The poorer accuracy of the SPIRE algorithm, however, appears to be due to entirely different reasons which are discussed in the next section.

For the January 1996 data, the results are poor for all three algorithms although MV and SPIRE appear to produce "cleaner" results in Figures 22 and 24, i.e. appear to track moving features with less scatter. The greater scatter in the MUSIC estimates is consistent with idea that MUSIC is too finely tuned for point-source signals.

Comparing the bearing estimates to the power levels shown in Figure 24c, the times of greatest bearing errors occurred when the signal power was low (less than 0 dB) indicating the utility of making these measurements as a means of qualifying the measurements.

Despite the worse than expected bearing accuracy, the SPIRE results do provide valuable insights into the signal environment. For example, from the power estimates for September 1995 data set, there appeared to be only one dominant signal scattering region active; generally in the great circle direction. This is in keeping with the expectation that the signal propagation condition would be benign for that given time period. However, comparing the region bearing estimates in Figure 23a and b to the signal bearing estimates in Figure 21a and b, indicates that the dominant region had a complex spatial power spectral shape (i.e. more than one peak) and that it was quite dynamic (i.e. the peaks changed location from estimate to estimate, especially the weaker peak).

Although the region bearing estimates in Figures 23 and 24 exhibit less scatter than the corresponding signal bearing estimates in Figures 21 and 22, the accuracy of the region bearing estimates appears to be worse overall. The weighted approach to estimating region bearings was based on the premise of a simple hill-like shape for the spatial power distribution of the scattering region. The complex shaped regions and dynamic nature of these regions may make the weighted approach too simplistic. Better accuracy may entail breaking complex shaped regions into subregions and then estimating the weighted bearing of each of these subregions.

Alternatively, the apparently poorer accuracy of the weighted region approach compared to the peak approach, and the apparently poorer accuracy of the SPIRE algorithm compared to the MV algorithm, may be a consequence of the effect of mutual coupling as discussed in the next section.
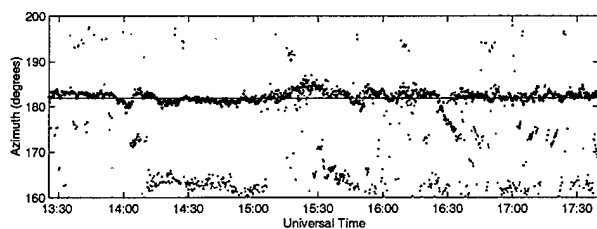
6.5 Problems with the Data

The apparently poorer than expected performance of the SPIRE algorithm, compared with the MV algorithm, suggests a possible problem with either the SPIRE signal model or the way the data was generated (equipment problems). To address this issue,
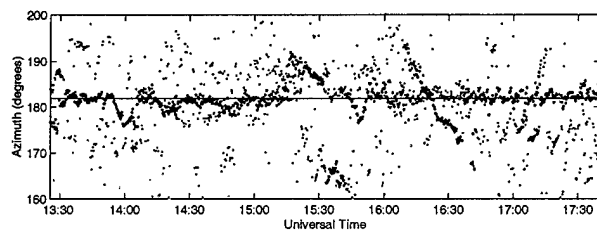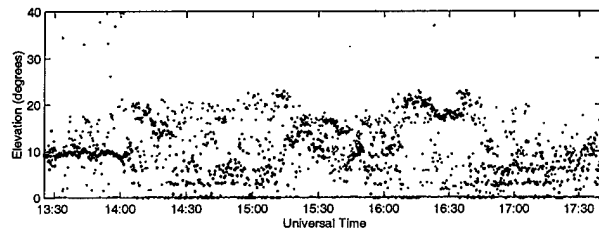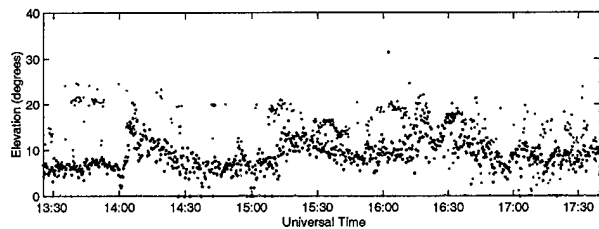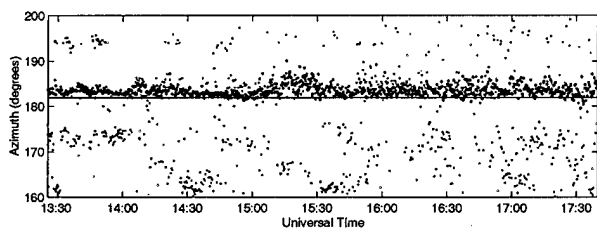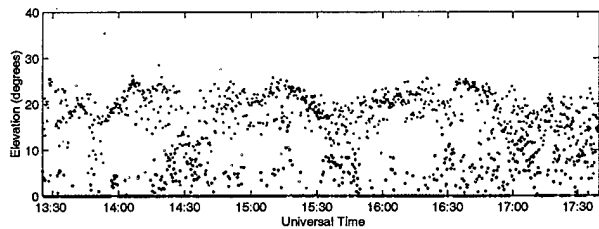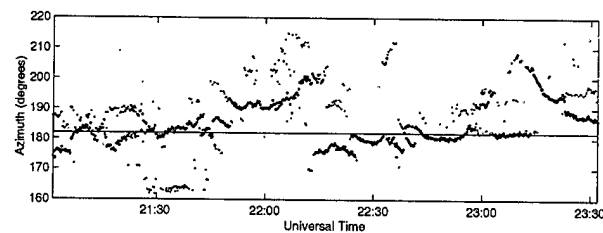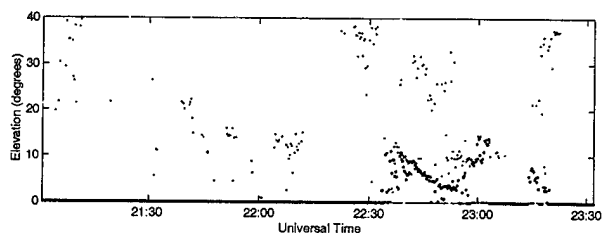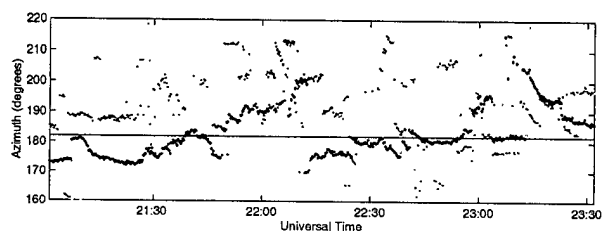
Figure 21: Azimuth and elevation bearing results for HF high latitude off-air data collected on September 2, 1995 using the SPIRE, MV algorithm and MUSIC algorithms. The azimuth bearing estimates are shown in (a) for SPIRE, (c) for MV, and (e) for MUSIC. The corresponding elevation bearing estimates are shown in (b), (d), and (f), respectively. Only the two strongest signals are shown with black representing the stronger of the two signals and red representing the weaker of the two. The solid horizontal lines in (a), (c), and (e) represent the great circle bearing.

Figure 22: *Azimuth and elevation bearing results for HF high latitude off-air data collected on September 2, 1995 using the SPIRE, MV algorithm and MUSIC algorithms. The azimuth bearing estimates are shown in (a) for SPIRE, (c) for MV, and (e) for MUSIC. The corresponding elevation bearing estimates are shown in (b), (d), and (f), respectively. Only the two strongest signals are shown where black represents the stronger of the two signals and red represents the weaker of the two. The solid horizontal lines in (a), (c), and (e) represent the great circle bearing.*
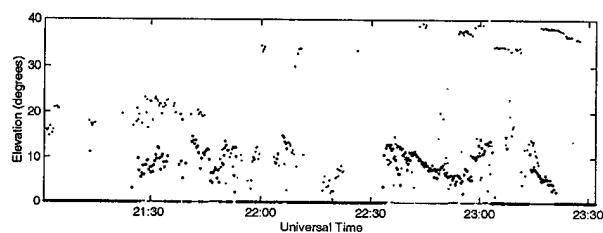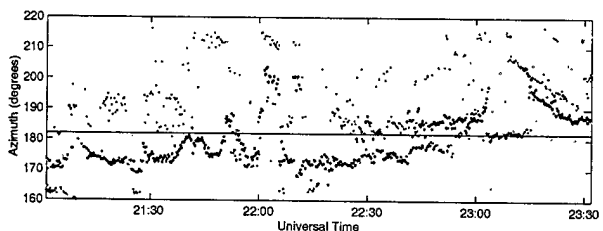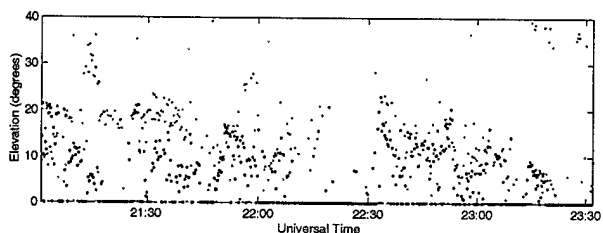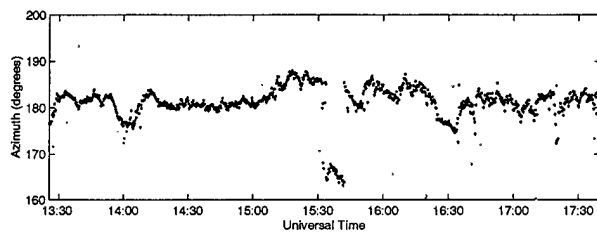
46

(a)
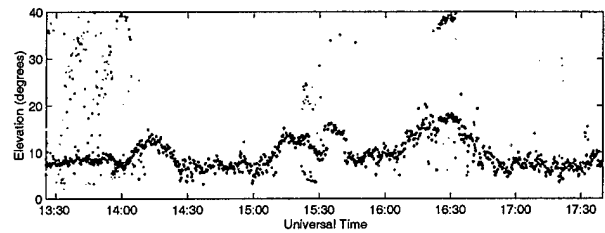
(b)
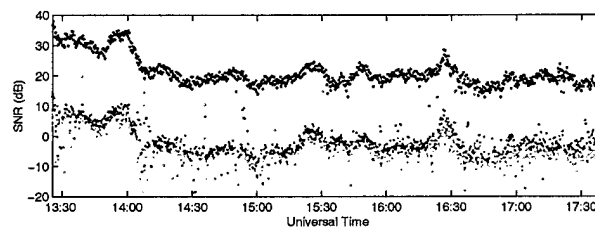
(c)

Figure 23: *More results of processing the January 24, 1996 data using the SPIRE algorithm and showing the estimated (a) region azimuth bearings, (b) region elevation bearings, and (c) region signal-to-noise levels. Only the four strongest regions are shown and they are colour coded black, red, orange, and yellow with black representing the strongest region and yellow the weakest region.*

(a)

(b)

(c)

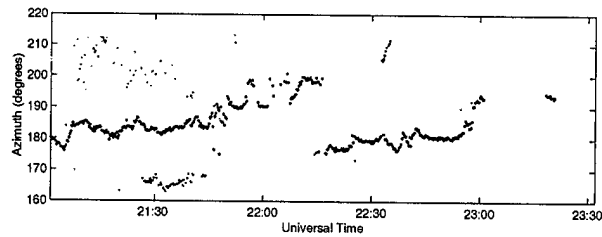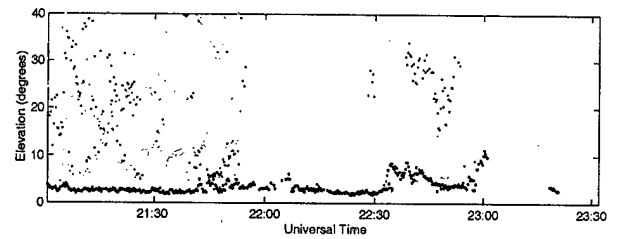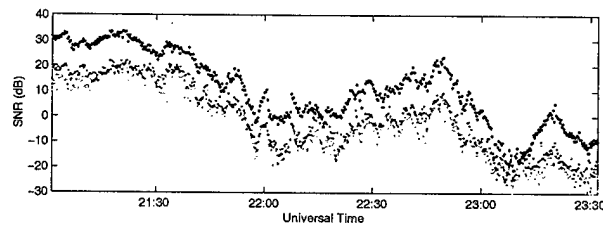*Figure 24:* *More results of processing the January 24, 1996 data using the SPIRE algorithm and showing the estimated (a) regions azimuth bearings, (b) region elevation bearings, and (c) region signal-to-noise levels. Only the four strongest regions are shown and they are colour coded black, red, orange, and yellow with black representing the strongest region and yellow the weakest region.*

several different aspects of model and data generation were investigated, namely, signal correlation and sample size, spacing and position of the signal model grid, and mutual coupling.

6.5.1 Testing Signal Correlation

The amount of data used to generate each data covariance matrix was assumed to be sufficient for decorrelation of the signal across each region. To test the validity of this assumption, varying amounts of the September 1995 data were used to generate the data covariance estimates and then the SPIRE error level determined. Repeating this 100 times for each sample size, the averaged model error results are shown in Figure 25.
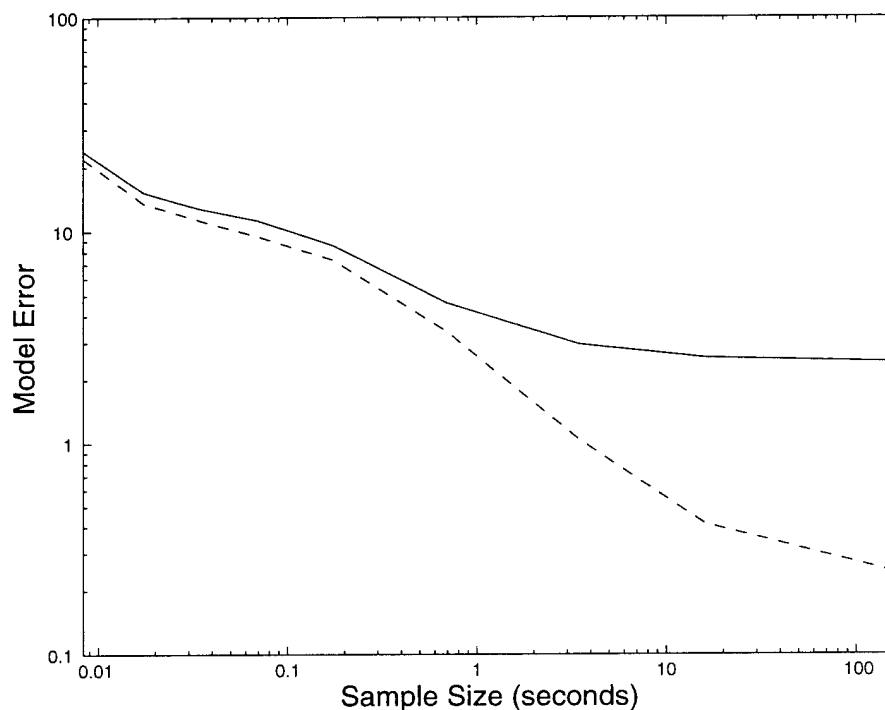
Figure 25: *Model error as a function of sample size. The upper curve (solid line) shows the results when the September 2, 1995 data is processed. The lower curve (dashed line) shows the simulated results.*

To provide a reference for comparison purposes, simulated data was also generated and the averaged model error computed in the same way. The simulated data was generated according to the expression

$$(54) \qquad \mathbf{X} = \mathbf{W}_s \mathbf{N}_1 + \mathbf{W}_n \mathbf{N}_2$$

where the spatial filter matrices were defined as

$$(55) \qquad \mathbf{W}_s = (\mathbf{C} - \sigma^2 \mathbf{R}_n)^{\frac{1}{2}}$$

$$(56) \qquad\qquad \mathbf{W}_n = \mathbf{R}_n^{\frac{1}{2}}$$

and $\mathbf{N}_1$ and $\mathbf{N}_2$ were spatially white noise matrices. The quantity $\mathbf{C} - \sigma^2\mathbf{R}_n)$ was the noise free signal model estimated by the SPIRE algorithm from an arbitrary sample of the actual data (sample length of 16 seconds). The time domain data in the rows of $\mathbf{N}_1$ was filtered to have the same spectral characteristics shown in Figure 26, which is an example of the spectral characteristics of the CFH signal when a single tone was being broadcast. The time domain data in the rows of $\mathbf{N}_2$ was not filtered (white noise only).

(a)
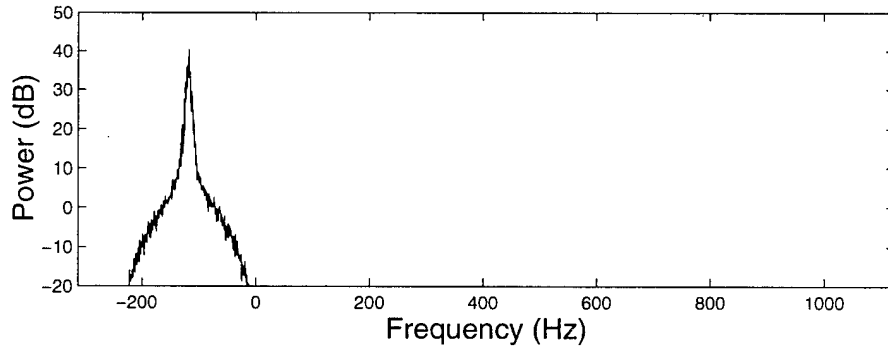
(b)

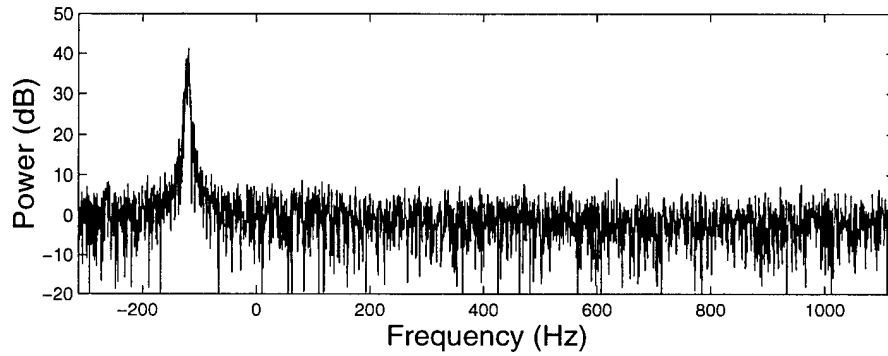**Figure 26:** *Spectral characteristics of the CFH signal are shown in (a) for an example time period when a single tone was being transmitted. The spectral characteristics of the filter used to replicate the signal part of the spectrum are shown in (b). The X-axis in both plots represents the frequency with respect to the center of the receiver passband.*

The purpose of generating the simulated data in the above way was to replicate, as closely as possible, the actual signal characteristics without violating the assumptions made about signal correlation. Hence $\mathbf{N}_1$ would have a much longer correlation constant than $\mathbf{N}_2$ due to the temporal filtering.

The model error results for the simulated data are shown in Figure 25. Comparing the actual and simulated results confirms that there is a problem with the model, but suggests that it was probably not due to insufficient correlation. For sampling times greater than about 1 second, the modeling error for the off-air data begins to flatten out while the modeling error for the simulated data continues to decrease. This might suggest that an extremely long correlation time was involved, however, even combining data from different days/months did not significantly reduce the model error showing that correlation was not the problem.

6.5.2 Testing the Model Grid

Another possible explanation is that the recorded signals in the data had a strong point-source component so that misalignment of the model grid contributed to the error, as discussed in Section 5.1. However, reducing the model grid spacing to 0.5 × 0.5 had no effect on the model error, nor did adjusting the grid up to ±0.5° in azimuth and elevation – essentially ruling out misalignment as the source of model error.

6.5.3 Testing for Coupling Effects

Having ruled out problems which could be mitigated by appropriately processing the data, the most likely problem was antenna coupling with the local environment (local site multipath) as well as coupling with other antennas in the array (mutual coupling). Coupling problems were extremely likely given that the local terrain was neither perfectly flat nor the ground perfectly conducting (frozen ground has low conductivity), and that the antennas in the inner Pusher ring are spaced closer than 1/4 wavelengths at 10.9445 MHz, virtually guaranteeing antenna to antenna coupling.

To investigate further, the effects of antenna coupling were added to the simulation models using the method outlined in [19] where impedances were calculated using the approach in [20]. At best, this can only be considered an approximation since the antenna is modeled to be an ideal monopole on a perfectly conducting ground. In reality, the antennas were elevated feed monopoles on poorly conducting ground. Hence, the main purpose of the simulation was to highlight the kinds of errors that multipath causes, not replicate the exact errors that actually occurred.

Using modeling errors as a guide, the initial simulations showed that the modeled mutual coupling voltage levels were too high, so these levels were reduced to 30% of their unmodified values. Using this adjusted mutual coupling model, the theoretical effect of sample size on model error is shown in Figure 27. In this case there is much better agreement between the

simulated results and the actual results than in Figure 25 strongly implicating antenna coupling as the source of errors.
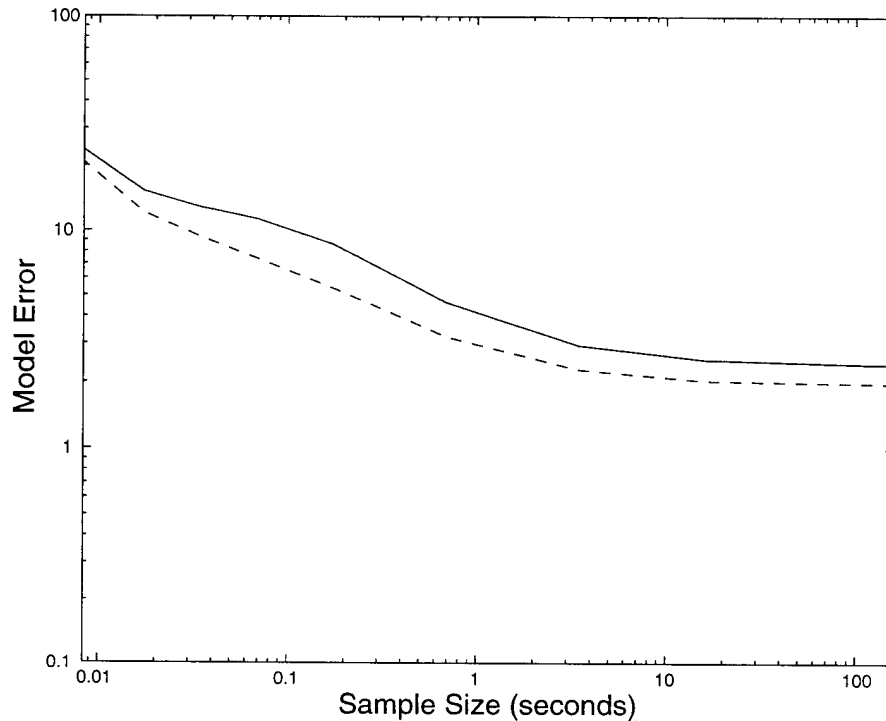

Figure 27: *Model error as a function of sample size. The upper curve (solid line) shows the results when the September 2, 1995 data is processed. The lower curve (dashed line) shows the simulated results when mutual coupling effects are included.*

To illustrate how modeling errors translate into bearing errors, an example of the effects of mutual coupling on the SPIRE estimated power spectrum is shown in Figure 28b. Comparing this to the ideal spectrum in Figure 28a, the major effect observed is the distortion of the shape of the signal region and the introduction of false regions. The shape distortion leads to biasing in the bearing estimates while the false regions leads to false estimates (i.e. wild bearings). In the worse case, distortion can lead to extra peaks in the main signal region causing potential errors for peak search methods.

Given the distorting effects of antenna coupling, it would be reasonable to suggest that the complex nature of the power spectrum shown for the off-air example Figure 28c was mainly due to the effect of multipath – the true power spectrum being simpler in nature. Unfortunately, the evidence is not strong enough to make this assessment with any certainty.

More compelling evidence is shown in Figure 29. Five hundred samples of data were generated using the same signal model used in Figure 28 (including the mutual coupling effects) except that the azimuth bearing was slowly
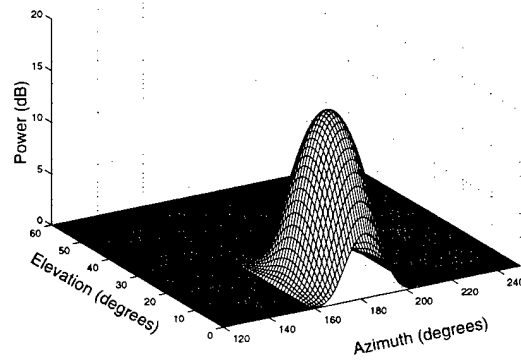
(a)
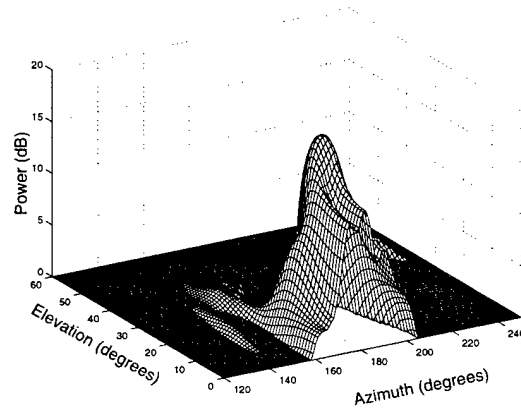
(b)
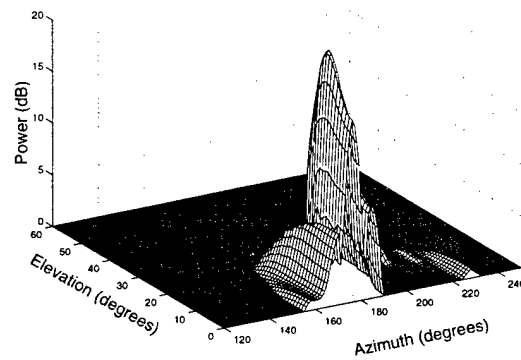
(c)

Figure 28: The effect of mutual coupling showing (a) the spatial power spectrum for a simulated signal, (b) the estimated SPIRE spectrum when mutual coupling is introduced, and (c) the estimated SPIRE spectrum for real data (a sample from the September 1995 data).

changed from 171.9° to 191.9° in a uniform manner. Estimates were made using the SPIRE algorithm (weighted and peak approach) and the MV algorithm. The true bearing is shown as the solid line in each of the plots.

The most remarkable thing about these results is that for samples 150 to 500 the MV algorithm produced estimated bearings of 180° ± 1° even though the actual bearings changed from 175.9° to 191.9°. This "flattening" effect is also apparent for the SPIRE algorithm results when the peak method was used, but not as severe. When the weighted region method was used, the flattening effect disappears. There is some biasing of up to 0.5°, but this is substantially less than the results for the peak method or the MV algorithm.

The main implication is that the superior performance of the MV algorithm for the off-air data (particularly the September 1995 data), might conceivably have been an illusion. That is, it is entirely possible that the great circle bearing was coincidentally favoured due to the effects of mutual coupling making the MV results appear better than they should have been.

Regardless of the relative performances observed, it seems highly probable that the results for all the algorithms were adversely affected by mutual coupling. Hence, a more accurate assessment of algorithm performance is not possible unless coupling effects can be calibrated. Ideally, this could have been accomplished using an airborne transmitter to measure the antenna array response as a function of azimuth and elevation angles for each frequency of interest. Unfortunately, due to logistical and cost reasons, this wasn't done. Calibration methods based on the data itself have been developed, but to the author's knowledge, none are appropriate for the high latitude signal environment. Hence more research is required in this area.
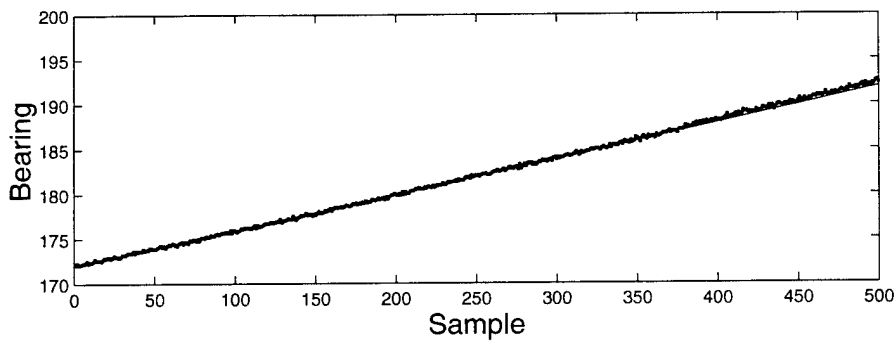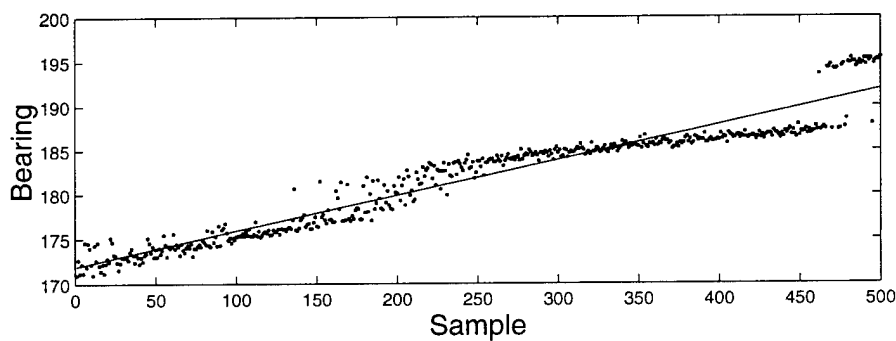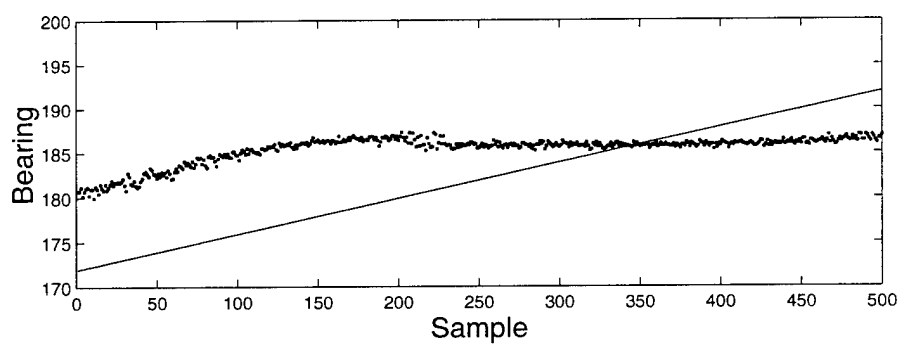
Figure 29: The effect of mutual coupling on bearing estimation for a moving spread-source showing the azimuth bearings estimates for (a) the SPIRE algorithm using the weighted region approach, (b) the SPIRE algorithm using the peak approach, and (c) the MV algorithm. The true bearings are shown by the solid line.

7. CONCLUSIONS AND RECOMMENDATIONS

The *SP*atial *I*ncoherent *R*egion *E*stimator (SPIRE) is a new algorithm based on maximum likelihood principles which was developed to estimate the spatial power spectrum using measurements from an N-channel antenna array. The algorithm is distinguished from other spectral estimation algorithms in that it assumes that all signals are uncorrelated but makes no assumption about their spatial shape and power distribution.

Several user controlled aspects of the algorithm were examined through simulation testing. This included resolving spatial ambiguities, determining the most appropriate grid spacing for the signal model and the minimum sampling size, and exploring the limit on the maximum number of signals that could be handled.

The testing showed that the easiest way to deal with spatial ambiguities is by choosing the simplest signal model which fits the data. The testing also showed that the grid spacing and sampling size parameters could be varied for a range of values over which estimation performance was either virtually unaffected or predictable. Additionally, it was also shown that the SPIRE algorithm can estimate a greater number of signals than there are antennas in the antenna array, exceeding the traditional $N - 1$ limit (where N is the number of antennas). However, practically speaking, remaining below this limit is more advisable.

Simulation testing of the SPIRE algorithm was also carried out to evaluate its performance as a function of various environmental conditions. This included the effect of noise, signal spreading, and the detection of a weaker signal in the presence of a stronger signal. In all cases, the performance of the SPIRE algorithm was predictable. Accuracy was similar to other superresolution algorithms when dealing with signals with no spatial spreading, but better when there was spreading.

Finally, testing was performed using off-air data collected at the Arctic site CFS Alert. The results were inconclusive as antenna mutual coupling effects were found to have corrupted the data. The analysis of the data did, however, showcase the advantages of the SPIRE algorithm in helping diagnose the non-ideal nature of the off-air data.

Generally it was demonstrated that the SPIRE algorithm is able to estimate the spatial power spectrum of the radio environment with a higher resolution and better accuracy than previously possible. As an analytical tool, the SPIRE algorithm provides a powerful new method for analyzing the spatial nature of signals, as well as a means of detecting data and equipment problems. Although originally developed for the high latitude HF signal environment, the algorithm can be applied to any N-channel data set provided the signals are uncorrelated both temporally and spatially.

Mutual coupling of antennas in the measurement array remains a problem. Although there is reason to believe that the SPIRE algorithm may be less sensitive to mutual coupling problems than other algorithms, it is still adversely affected. For the high

latitude HF measurements made from CFS Alert in the mid 1990's, calibrating the coupling effects is of paramount importance if the potential usefulness of this data set is ever to be realized. Since no in situ calibration was ever done, calibration would involve deriving the correction coefficients from the data itself. Unfortunately no good method has been developed to do this kind of calibration, so continued research in this area is required. Additionally, since in situ calibration is often expensive and difficult, many modern DF systems would also benefit greatly from this kind of research.

References

1. Dumas, D.J., "High-Latitude HF Direction Finding: A Case Study and Modeling Results", Second Symposium on Radiolocation and Direction Finding, Southwest Research Institute, San Antonio, Texas, November 1997.

2. Jenkins, R.W., "Preliminary Analysis of Kestrel Data", Department of Communications/Communications Research Centre, Tech. Memo DRL/TM083/92, February 1992.

3. Read, W.J.L., "A Maximum Likelihood HF Direction Finding Estimator for High Latitude Distributed Signals", Defence Research Establishment Ottawa, Tech. Report 1999-085, April 1999.

4. Jenkins, R.W., "Comparison of Spread and Point-Source Multiple-Direction Estimation Techniques for High Latitude HF Direction-Finding", Communications Research Centre, Technical Note No. 98-002, April 1998.

5. Marple, S.L., *Digital Spectral Analysis with Applications*, Alan Oppenheim, editor, Prentice-Hall, Englewood Cliffs, New Jersey, Chapter 4, 1987.

6. Chan, A.J., "Application of High-Resolution Techniques to the Joint AEDOA Estimation with a Uniform Circular Array", Master Thesis, McMaster University, Hamilton, December 1991.

7. Stoica, P., Sharman, K.C., "Maximum Likelihood Methods for Direction-of-Arrival Estimation", *IEEE Transactions on Acoustics, Speech, and Signal Processing*, Vol. 38, No. 7, July 1990.

8. Bohme, J.F., "Source-Parameter Estimation by Approximate Maximum Likelihood and Nonlinear Regression", *IEEE Journal of Oceanic Engineering*, Vol. 10, No. 3, July 1985.

9. Hung, E.K., Hu, Z., "Analysis of the HF Data Measured at Leitrim, Using a Matrix Calibration Method Developed at DREO", Defence Research Establishment Ottawa, Tech. Report DREO-1319, November 1997.

10. Dumas, D.J., "Direction Finding Algorithms and Software for a Sampled-Aperture Antenna Array Operating at High Latitudes in the HF Band", Industry Canada/Communications Research Centre, Tech. Memo VPRB 03/98, March 1998.

11. Jenkins, R.W., "A Field-Aligned Scattering Model for High-Latitude Propagation", Department of Communications/Communications Research Centre, Tech. Memo DRL/TM095/92, December 1992.

12. Capon, J., "High-Resolution Frequency-Wavenumber Spectrum Analysis", *Proceedings of the IEEE*, Vol. 57, August 1969.

13. Protter, M.H., and Morrey, C.B.,*Modern Mathematical Analysis*, Lynn Loomis, editor, Addison-Wesley Publishing Company, Reading, Mass., Chapter 4, 1964.

14. Schmidt, R.O., "Multiple Emitter Location and Signal Parameter Estimation", *IEEE Transactions on Antennas and Propagation*, Vol. 34, No. 3, March 1986.

15. Ziskind, I., and Wax, M., "Maximum Likelihood Localization of Multiple Sources by Alternating Projection", *IEEE Transactions on Acoustices, Speech, and Signal Processing*, Vol. 36, No. 10, October 1988.

16. Jenkins, R.W., "Effects of Antenna Array Geometry and Element Pattern Uncertainty on High-Latitude HF Direction Finding", Communications Research Centre, Report No. 97-006, December 1997.

17. Wax, M., and Kailath, T., "Detection of Signals by Information Theoretic Criteria", *IEEE Transactions on Acoustics, Speech, and Signal Processing*, Vol. 33, No. 2, April 1985.

18. Jones, T.B., Warrington, E.M., Rogers, N.C., Hamadyk, P., "Simultaneous Oblique Sounding and Bearing Measurements of HF Radio Waves Received Over High Latitude Paths", *Second Symposium on Radiolocation and Direction Finding, Proceedings*, Vol. 1, Session 1, Paper 1, November 4-6, 1997.

19. Read, W.J.L., "The Effects of the Environment on an Experimental VHF Radio Direction Finding Antenna System", Defence Research Establishment Ottawa, Tech. Report 1226, August 1994.

20. Brown, G.H., and King, R., "High-Frequency Models in Antenna Investigations", *Proceedings of the Institute of Radio Engineers"*, Vol. 22, No. 4, April 1934.

DOCUMENT CONTROL DATA

(Security classification of title, body of abstract and indexing annotation must be entered when the overall document is classified)

1. ORIGINATOR (the name and address of the organization preparing the document. Organizations for whom the document was prepared, e.g. Establishment sponsoring a contractor's report, or tasking agency, are entered in section 8.)	2. SECURITY CLASSIFICATION (overall security classification of the document, including special warning terms if applicable)
DEFENCE RESEARCH ESTABLISHMENT OTTAWA DEPARTMENT OF NATIONAL DEFENCE OTTAWA, ONTARIO, K1A 0Z4	UNCLASSIFIED

3. TITLE (the complete document title as indicated on the title page. Its classification should be indicated by the appropriate abbreviation (S,C or U) in parentheses after the title.)

   A SPATIAL POWER SPECTRUM ESTIMATOR FOR DISTRIBUTED SIGNALS (U)

4. AUTHORS (Last name, first name, middle initial)

   READ, WILLIAM, J.L.

5. DATE OF PUBLICATION (month and year of publication of document) DECEMBER 2000	6a. NO. OF PAGES (total containing information. Include Annexes, Appendices, etc.) 59	6b. NO. OF REFS (total cited in document) 20

7. DESCRIPTIVE NOTES (the category of the document, e.g. technical report, technical note or memorandum. If appropriate, enter the type of report, e.g. interim, progress, summary, annual or final. Give the inclusive dates when a specific reporting period is covered.)

   DREO TECHNICAL REPORT

8. SPONSORING ACTIVITY (the name of the department project office or laboratory sponsoring the research and development. Include the address.)

   DEFENCE RESEARCH ESTABLISHMENT OTTAWA
   DEPARTMENT OF NATIONAL DEFENCE
   OTTAWA, ONTARIO, K1A 0Z4

9a. PROJECT OR GRANT NO. (if appropriate, the applicable research and development project or grant number under which the document was written. Please specify whether project or grant) 5BD15	9b. CONTRACT NO. (if appropriate, the applicable number under which the document was written)
10a. ORIGINATOR'S DOCUMENT NUMBER (the official document number by which the document is identified by the originating activity. This number must be unique to this document.) DREO TECHNICAL REPORT 2000−099	10b. OTHER DOCUMENT NOS. (Any other numbers which may be assigned this document either by the originator or by the sponsor)

11. DOCUMENT AVAILABILITY (any limitations on further dissemination of the document, other than those imposed by security classification)

(X) Unlimited distribution
( ) Distribution limited to defence departments and defence contractors; further distribution only as approved
( ) Distribution limited to defence departments and Canadian defence contractors; further distribution only as approved
( ) Distribution limited to government departments and agencies; further distribution only as approved
( ) Distribution limited to defence departments; further distribution only as approved
( ) Other (please specify):

12. DOCUMENT ANNOUNCEMENT (any limitation to the bibliographic announcement of this document. This will normally correspond to the Document Availability (11). However, where further distribution (beyond the audience specified in 11) is possible, a wider announcement audience may be selected.)

   UNLIMITED

13. ABSTRACT (a brief and factual summary of the document. It may also appear elsewhere in the body of the document itself. It is highly desirable that the abstract of classified documents be unclassified. Each paragraph of the abstract shall begin with an indication of the security classification of the information in the paragraph (unless the document itself is unclassified) represented as (S), (C), or (U). It is not necessary to include here abstracts in both official languages unless the text is bilingual).

This report details the development of an N-channel spatial power spectrum estimation technique called the SPatial Incoherent Region Estimator (SPIRE). It was developed in support of research aimed at characterizing the spatial spreading of HF signals caused by the high latitude propagation environment with the ultimate goal of improving high latitude HF radio direction finding performance. Based on the assumption of temporal and spatial incoherence, SPIRE uses a surprisingly simple, yet effective, approach based on maximum likelihood principles to model the spatial power spectrum. The result is an algorithm which provides a more accurate and more informative characterization of the spatial nature of incoming signals than currently popular conventional and modern superresolution algorithms. This characterization includes bearing, spatial extent and power distribution, and total power of the signal. It also includes total noise power and modeling accuracy. The performance and utility of the SPIRE algorithm is demonstrated using both simulation and off-air data.

14. KEYWORDS, DESCRIPTORS or IDENTIFIERS (technically meaningful terms or short phrases that characterize a document and could be helpful in cataloguing the document. They should be selected so that no security classification is required. Identifiers such as equipment model designation, trade name, military project code name, geographic location may also be included. If possible keywords should be selected from a published thesaurus. e.g. Thesaurus of Engineering and Scientific Terms (TEST) and that thesaurus-identified. If it is not possible to select indexing terms which are Unclassified, the classification of each should be indicated as with the title.)

RADIO DIRECTION FINDING
SUPERRESOLUTION
HF
MINIMUM VARIANCE
MUSIC
MAXIMUM LIKELIHOOD
HIGH LATITUDE SIGNALS
IONOSPHERIC PROPAGATION
N CHANNEL
ANTENNA ARRAY